Computers and Chemical Engineering 174 (2023) 108196

Contents lists available at ScienceDirect

Computers and Chemical Engineering

journal homepage: www.elsevier.com/locate/compchemeng

A generalized disjunctive programming model for the optimal design of reverse electrodialysis process for salinity gradient-based power generation

C. Tristán [a,*], M. Fallanza [a], R. Ibáñez [a], I. Ortiz [a], I.E. Grossmann [b]

[a] Department of Chemical and Biomolecular Engineering, University of Cantabria, Av. Los Castros 46, Santander 39005, Spain
[b] Department of Chemical Engineering, Carnegie Mellon University, Pittsburgh, PA 15213, USA

ARTICLE INFO

Keywords:
Salinity gradient energy
Renewable electricity
Superstructure optimization
Net present value
Levelized cost of energy
Global logic-based outer approximation algorithm

ABSTRACT

Reverse electrodialysis (RED) is an emerging electro-membrane technology that generates electricity out of salinity differences between two solutions, a renewable source known as salinity gradient energy. Realizing full-scale RED would require more techno-economic and environmental assessments that consider full process design and operational decision space from the RED stack to the entire system. This work presents an optimization model formulated as a Generalized Disjunctive Programming (GDP) problem that incorporates a finite difference RED stack model from our research group to define the cost-optimal process design. The solution to the GDP problem provides the plant topology and the RED units' working conditions that maximize the net present value of the RED process for given RED stack parameters and site-specific conditions. Our results show that, compared with simulation-based approaches, mathematical programming techniques are efficient and systematic to assist early-stage research and to extract optimal design and operation guidelines for large-scale RED implementation.

1. Introduction

Dispatchable low-carbon sources of power are essential to meet flexibility constraints in clean energy transitions (Davis et al., 2018). Salinity gradient energy (SGE), or the free energy released during the mixing of high salinity and low salinity waters (Pattle, 1954), is a vast yet largely untapped renewable source that can buffer the hour-to-hour variability of intermittent renewable power sources. According to Gibbs free energy of mixing, each cubic meter of river water (1.5 mM NaCl) flowing into the sea (0.6 M NaCl) stores 0.44 kWh of baseload and non-pollutant extractable energy (Yip et al., 2016). It is estimated that about 1.4 to 1.7 TW is available globally from major river mouths (Alvarez-Silva et al., 2016; Ramon et al., 2011), of which ~60% could be harnessed depending on SGE conversion efficiency, siting constraints, freshwater availability, and environmental and legal constraints (Alvarez-Silva et al., 2016; Kuleszo et al., 2010; Ramon et al., 2011). Alternatively, anthropogenic waste streams of energy-intensive processes such as desalination's concentrates, reclaimed wastewater effluents, produced waters (a by-product of oil and gas extraction), or thermolytic salt solutions in energy storage and close-loop applications that recover low-grade waste heat energy, promise higher SGE (Tian et al., 2020; Tufa et al., 2018; Yip et al., 2016). For instance, seawater desalination brine (1.2 M NaCl) mixed with low salinity effluent from wastewater treatment (10 mM), almost doubles the seawater-river water pair's SGE, e.g., 0.85 kWh per m^3 of low salinity stream (Yip et al., 2016). Global wastewater discharge into the sea could provide another 18.5 GW of salinity-gradient power (Ramon et al., 2011).

There are different technologies to capture SGE reported in the literature (Logan and Elimelech, 2012; Yip et al., 2016), among them reverse electrodialysis (RED) and pressure retarded osmosis (PRO) are in advanced development stages and have been demonstrated at pilot-scale (IRENA, 2020; Jang et al., 2020; Kempener and Neumann, 2014; Makabe et al., 2021; Mehdizadeh et al., 2021; Nam et al., 2019; Pärnamäe et al., 2020; Post et al., 2010; Tedesco et al., 2017). Both technologies use selective membranes to draw electricity out of the reversible mixing between high and low salinity streams. RED is an electrochemical technology that uses ion-exchange membranes (IEM) to directly generate electricity from chemical potential differences between the two salt-differing water solutions (Pattle, 1954). A RED stack (Fig. 1) comprises a series of repeating cell pairs framed on either side by electrodes. Each cell pair is made up of a cation-exchange membrane (CEM), an anion-exchange membrane (AEM), and two spacers in between to form alternate compartments where the high and low concentration streams flow. The IEMs allow selective permeation of

* Corresponding author.
E-mail address: tristanc@unican.es (C. Tristán).

https://doi.org/10.1016/j.compchemeng.2023.108196
Received 13 November 2022; Received in revised form 10 February 2023; Accepted 17 February 2023
Available online 18 February 2023
0098-1354/© 2023 The Author(s). Published by Elsevier Ltd. This is an open access article under the CC BY-NC-ND license (http://creativecommons.org/licenses/by-nc-nd/4.0/).

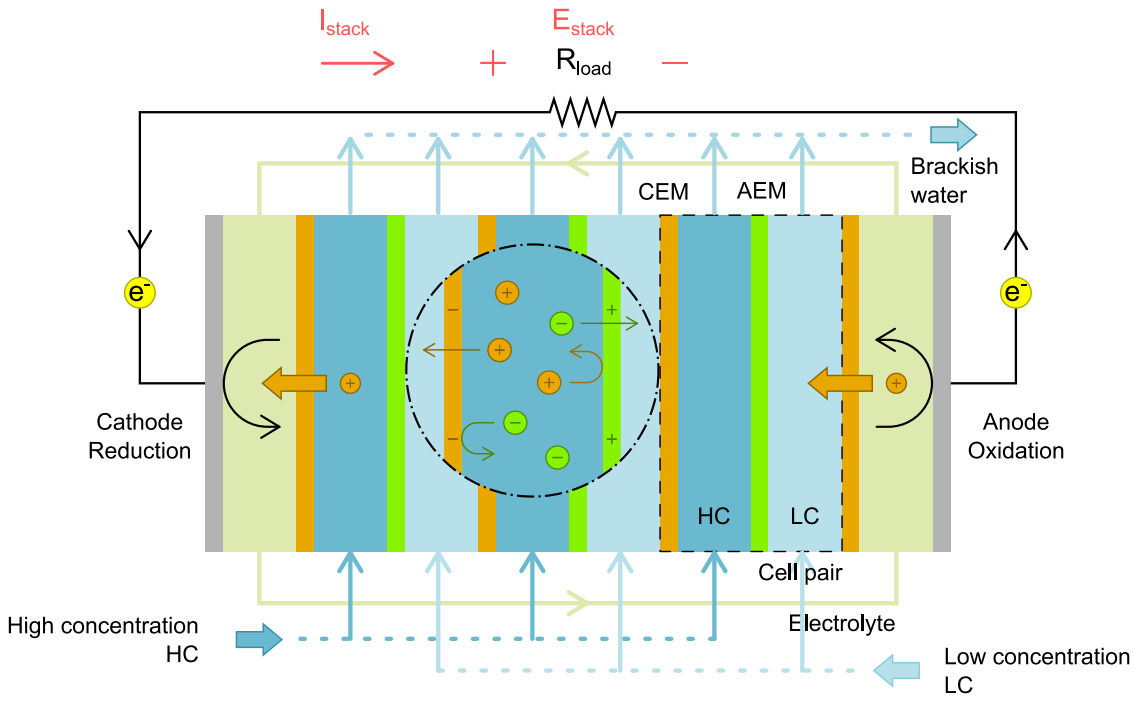

Fig. 1. Working principle of reverse electrodialysis (RED). CEM: Cation-exchange membrane; AEM: Anion-exchange membrane.

opposite-charged ions (counterions) while rejecting water and like-charged ions (co-ions). The concentration difference across the IEMs creates an electrochemical potential that drives the diffusion of cations across CEMs towards the cathode, and anions across AEMs towards the anode, from the high concentration (HC) to the low concentration (LC) solutions. Redox reactions at the electrodes convert the directional flow of ions into an electric current; the electric current and the electric potential yielded by the RED pile can then be used to power the external load connected to the electrodes (Pattle, 1954).

Several authors have developed predictive models to fully capture the RED stack performance (Tristán et al., 2020a). Early modeling approaches dating back to the '80s (Lacey, 1980; Weinstein and Leitz, 1976) were updated and refined thereafter to consider non-idealities (e.g., concentration polarization, electric short-cut currents, electrode system resistance) (Culcasi et al., 2020; Gurreri et al., 2014; La Cerva et al., 2017; Ortiz-Imedio et al., 2019; Pawlowski et al., 2016; Post et al., 2008; Tedesco et al., 2015a; Tristán et al., 2020a; Veerman et al., 2008), complex geometries (e.g., spacers' designs or profiled membranes) (Ciofalo et al., 2019; Dong et al., 2022; Faghihi and Jalali, 2022; Gurreri et al., 2017; Kim et al., 2022; Pawlowski et al., 2016), flow patterns (e.g., co-, counter-, and cross-flow stacks) (Pintossi et al., 2021; Simões et al., 2020; Tedesco et al., 2015b; Vermaas et al., 2013), advanced electrode systems (e.g., electrode segmentation) (Kim et al., 2022; Pintossi et al., 2021; Simões et al., 2020; Veerman et al., 2011), and the presence of organic and inorganic pollutants and multi-valent ions on feed solutions (Gómez-Coma et al., 2019; Pintossi et al., 2021; Simões et al., 2022).

The membrane power density, i.e., the power generated per total membrane area, the specific energy, i.e., the energy delivered per volume of HC and/or LC feedwater consumed, and the energy efficiency, i.e., the salinity gradient energy converted into useful work, are well-accepted metrics to assess RED energy production feasibility as they implicitly inform about its cost-competitiveness. Optimization studies mainly focus on the design and working conditions that maximize these key performance metrics, but few consider cost metrics (e.g., levelized cost of electricity and capital costs per unit of power) that are the primary drivers of technology adoption in any sector (Daniilidis et al., 2014; Giacalone et al., 2019; Papapetrou et al., 2019; Weiner et al., 2015). Genetic algorithms (Faghihi and Jalali, 2022; Long et al., 2018a, 2018b), gradients-ascent algorithms (Ciofalo et al., 2019), and response surface methods with a central composite design (Altıok et al., 2022) are some of the approaches to solve single and multi-objective optimization problems, to define designs and operating conditions that maximize the net power density (Altıok et al., 2022; Ciofalo et al., 2019; Long et al., 2018b), maximize the mass transfer and minimize the pressure drop in the RED cell (Faghihi and Jalali, 2022), or maximize the net power density and energy efficiency (Long et al., 2018a) of the RED stack.

Few works address the synthesis and design of the RED process featuring these predictive models to devise technically and economically feasible flowsheet designs. Most of the reported studies in the open literature investigate the RED process as a separate unit or several units in either series or simple arrangements, focusing primarily on improving the power density and/or the energy conversion efficiency of RED. There is an intrinsic trade-off between efficiency and power of RED stack as maximizing both would require conflicting operating conditions, multi-staging or cascade operation and electrode segmentation of the RED stacks could attain efficient designs with higher power densities than once-through RED operation (Simões et al., 2021). Multi-stage RED adds several degrees of freedom, such as independent electrical control of the stages (Hu et al., 2020, 2019; Veerman, 2020) (as electrode segmentation offers), asymmetric staging, and different configurations (Tedesco et al., 2015b; Veerman, 2020; Veerman et al., 2009). Simões et al. (Simões et al., 2022, 2021, 2020) and Pintossi et al. (Pintossi et al., 2021) also investigated the effect of electrode segmentation and multi-staging of RED stacks under different flow configurations, both strategies provided higher power densities and energy efficiencies.

Full-scale RED progress demands more techno-economic and environmental assessments that consider full process design and operational decision space from stack to the whole system. These pioneering works evidence how challenging it is to model and estimate the cost of a complex system with interdependent processes and phenomena. Cost-optimization modeling can effectively assess the economic feasibility of RED as it can handle strongly coupled systems of equations with several degrees of freedom (Pistikopoulos et al., 2021). Hence, our aim is to develop a modeling tool to provide decision-making support from early-stage applied research to full-scale RED deployment in real scenarios. We present an optimization model formulated as a Generalized

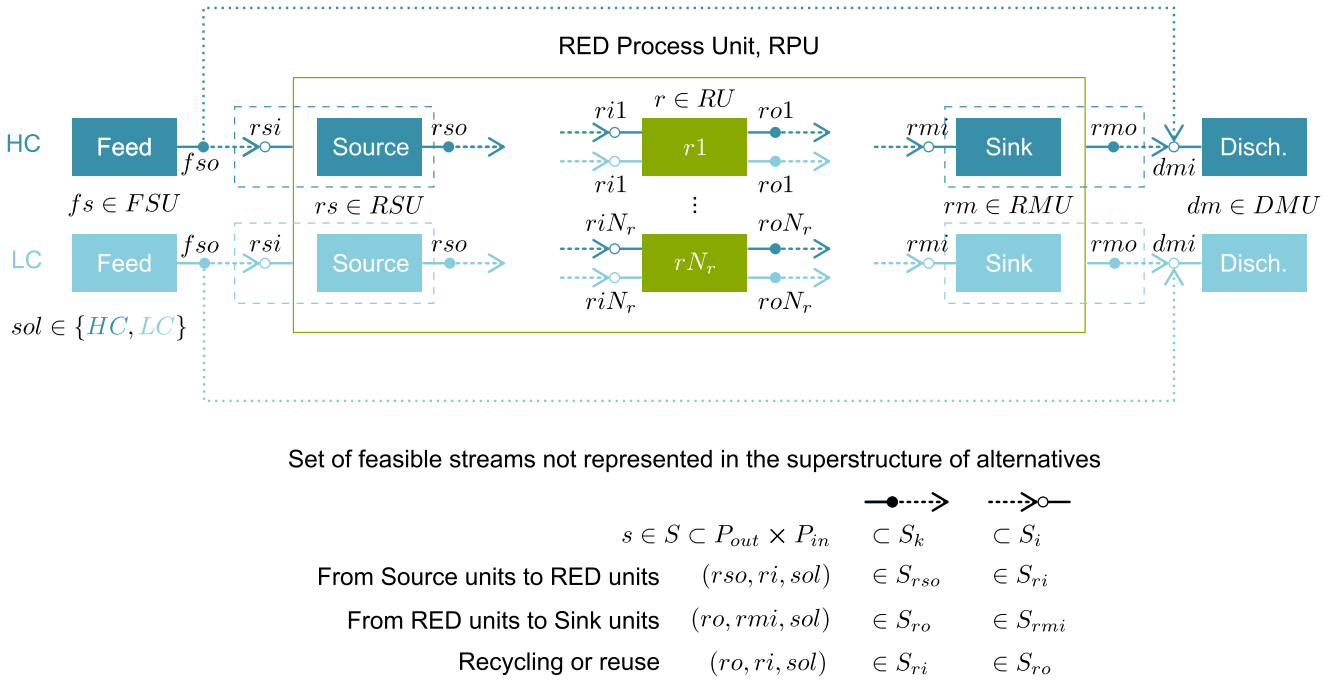

Fig. 2. Superstructure representation of the RED process with *Nr* conditional RED units. The set of source (*RSU*) and sink (*RMU*) units and the set of candidate RED units (*RU*) are children of the parent RED Process unit (*RPU*). Dashed boxes indicate the association between the set of source units with its parent ports, *rsi,* and the set of sink units with its parent ports, *rmo.* The whole set of units, ports, and streams and their index notation is in Table 1.

Table 1
Indices and sets of units, ports, and streams of the RED process superstructure.

Unit	Port		Streams $s \in S \subseteq P_{out} \times P_{in}$	
	In P_{in}	Out P_{out}	In $i \in S_i \subseteq S$	Out $k \in S_k \subseteq S$
Feed unit $fs \in FSU$	*fsi*	*fso*	*in,fsi* [b]	*fso,rsi* *fso,dmi*
Source unit $rs \in RSU$	*rsi*	*rso*	*fso,rsi*	*rso,ri*
RED unit [a] $r \in RU$	*ri*	*ro*	*rso,ri* *ro',ri* [c]	*ro,rmi* *ro,ri'* [c]
Sink unit $rm \in RMU$	*rmi*	*rmo*	*ro,rmi*	*rmo,dmi*
Discharge unit $dm \in DMU$	*dmi*	*dmo*	*fso,dmi* *rmo,dmi*	*dmo,out*

[a] When the RED unit is active (Y_r = True): $i = (r, ro)$ in (7), $k = (ri, r)$ in (8).
[b] Known feed streams composition and volume according to RED's implementation scenario.
[c] Recycle or reuse.

Disjunctive Programming (GDP) problem to define the cost-optimal RED process design for different deployment scenarios. The GDP optimization model incorporates a semi-rigorous version of our RED stack model (Gómez-Coma et al., 2019; Ortiz-Imedio et al., 2019; Ortiz-Martínez et al., 2020; Tristán et al., 2020a) to determine the flowsheet design that maximize the net present value of the RED process.

2. Problem statement and superstructure definition

Given the site-specific working conditions, i.e., concentration, total flowrate, and temperature of the HC and LC feedwaters, and the stack parameters of the RED units, i.e., number of cell pairs, properties of membranes and spacers, the problem is to determine the RED plant topology and the working conditions of each RED stack in the plant that maximize the net present value of the RED process.

In the quest to tackle water scarcity, seawater reverse osmosis (SWRO) desalination and re-use of reclaimed wastewater effluents stand out above all else (UNESCO, 2020; van Vliet et al., 2021). A foreseeable scenario for RED promotion is next to these energy-intensive processes (Rani et al., 2022) that are heavily reliant on fossil fuels (IEA, 2016). The SGE embodied in the reversible mixing of the high-saline SWRO brine and low-salinity stream as treated wastewater could partially displace the carbon-intensive grid mix supply of these processes. Besides, environmental and permitting challenges associated with brine discharge may incentivize RED technology mature. Hence, in all assessed scenarios, we assume the RED system recovers energy from a SWRO concentrate effluent (as HC feedstream) paired with a low-salinity water, e.g., freshwater, or reclaimed wastewater as LC feedstream.

We have defined the superstructure of alternatives based on the Pyosyn Graph (PSG) representation (Chen et al., 2021b). The RED process' PSG representation in Fig. 2 consists of the following elements:

(a) The RED Process Unit (RPU), where discrete decisions on the selection of the RED units are made, which embeds: (i) the set of N_r candidate RED units $r \in RU = \{r1 \ldots, rN_r\}$; the set of permanent (ii) source $rs \in RSU$ and (iii) sink $rm \in RMU$ units for the high-salinity and low-salinity streams, i.e., $sol \in SOL = \{HC, LC\}$. The source and sink units govern the material inflows and outflows at the interface of the RPU parent block with the overall flowsheet (i.e., with the feed and discharge units).
(b) The sets of concentrate and diluate feed units, $fs \in FSU$, and discharge units, $dm \in DMU$
(c) The inlet and outlet ports $p \in P = P_{out} \cup P_{in}$, i.e., mixers and splitters, where flows of material at the unit interface with other process units may take place.
(d) The set of streams or feasible outlet-to-inlet port pairs, $s \in S \subseteq P_{out} \times P_{in}$, defined considering the following screening rules:
- The feed units, *FSU*, supply the concentrate and diluate feed streams, $s \in S_{fso} \subseteq S_k$, to the RED Process Unit (RPU); the discharge units *DMU* collect the exhausted high- and low-concentration RPU effluents, and the unused feed streams from the feed units *FSU*, $s \in S_{dmi} \subseteq S_i$.

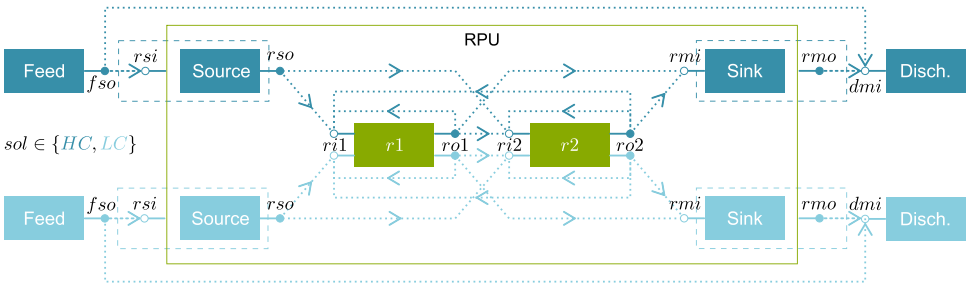

Fig. 3. Example of RED process' superstructure with two conditional RED units.

- Within the RPU, the source units, *RSU*, supply the concentrate and diluate streams coming from the feed units *FSU* to one or more of the active RED units, $s \in S_{rso} \subseteq S_k$. Once the active RED units exploit SGE from the inlet streams, $s \in S_{ri} \subseteq S_i$, the spent effluents, $s \in S_{ro} \subseteq S_k$, may be recycled back, sent to other active RED units for reuse, or may be directed to the sink units, *RMU*. The RPU effluent from *RMU*, $s \in S_{rmo} \subseteq S_k$, is disposed of in the overall discharge unit *DMU*.
- No flow between the *RSU* and *RMU* is allowed; it only can take place between *FSU* and *DMU*.
- Mixing between the concentrate and diluate streams only takes place within the candidate RED units owing to the flow of ions from high-salinity compartments to low-salinity ones through ion-exchange membranes (IEMs).

Table 1 summarizes the indices and sets of units, ports, and streams of the general superstructure in Fig. 2, and Fig. 3 shows an example with two candidate RED units.

3. Optimization model

3.1. Generalized disjunctive programming (GDP) model

The general form of the optimization model for the superstructure in Fig. 2, is formulated as a Generalized Disjunctive Programming (GDP) problem in (1).

$$
\begin{aligned}
\max obj \quad & = f(x) \\
s.t. \quad & g(x) \leq 0 \\
& \begin{bmatrix} Y_r \\ r_r(x) \ \leq \ 0 \end{bmatrix} \vee \begin{bmatrix} \neg Y_r \\ B^r \ x \ = \ 0 \end{bmatrix} \quad r \in RU \\
& \Omega(Y_r) = True \\
& x \in X \subseteq R^n \\
& Y_r = \{True, False\} \quad r \in RU
\end{aligned} \tag{1}
$$

The objective function $f(x)$ maximizes the Net Present Value (NPV) of the RED process subject to inequality constraints (e.g., process specifications) and equality constraints (e.g., material, energy balances, and thermodynamic relationships). The variables x describe continuous variables (e.g., molar concentrations, volumetric flows) of all feasible streams and internal variables of the candidate RED units (e.g., electric current). The global constraints, $g(x) \leq 0$, are equalities and inequalities describing specifications and physical relationships that apply for all feasible configurations in the superstructure, i.e., linking constraints, flow and mass balances of the feed, source, sink, and discharge units' inlet and outlet ports, and bounds on streams variables (concentration and flowrate). The disjunctions—corresponding to logical-XOR relationships such that at most one disjunct in each disjunction is True—describe the existence or absence of the RED units within the RED process unit. The Boolean variables Y_r indicates whether a given RED unit exists or not. If a unit exists (Y_r = True), the constraints $r_r(x) \leq 0$ enforce the relevant mass and energy balances, thermodynamics, kinetics, or other physical/chemical phenomena taking place within the RED unit; if the unit is absent, the negation ($\neg Y_r$) sets to zero a subset of the continuous variables, and cost terms in the objective function through the $B^r x = 0$ constraints.

When the RED unit ports exist, mixing and splitting calculations, and linking constraints, which equate stream flow properties between the RED unit's ports and its set of cell pairs, are included within the constraints $r_r(x) \leq 0$, and port absence in the linear constraints $B^r x = 0$. We adopt the no-flow approach for modeling an absent unit, enforcing that if a stream does not exist, no flow may take place between the corresponding outlet-inlet port pair.

The logical relationships ($\Omega(Y_r) = True$) establish the logic conditions for selecting the candidate RED units. In the following sections, we will present the detailed equations and constraints after stating the major assumptions.

3.2. Assumptions

We consider the following simplifying assumptions in the development of the GDP model:

(a) The feed streams are pure sodium chloride (NaCl), ideal aqueous solutions (i.e., activity coefficients equal to 1), thus neglecting the non-idealities of aqueous solution and the existence of other species that would undermine the RED performance.
(b) There is no non-ohmic contribution in the internal losses ascribed to concentration polarization phenomena in the concentrate and diluate membrane-solution interfaces, and due to concentration gradient decline along the main flow direction. We only consider the ohmic contribution of solutions' ionic conductivity and membranes' ionic resistance.
(c) Membranes' permselectivity and ionic resistance are constant regardless of solutions' concentration and temperature.
(d) There is no water transport due to osmosis from the low-salinity side to the high-salinity one across membranes, which implies a constant streamwise volumetric flowrate in RED's channel.
(e) Salt diffusivities in the membrane phase are constant whatever concentration and temperature.
(f) All cell pairs behave equally, as we assume no fluid leakage or ionic shortcut currents in the RED stack's manifolds.
(g) Co-current flow of the high- and low-concentration streams.
(h) The RED system operates under isothermal and isobaric conditions.

3.3. RED stack model

We use a semi-rigorous version of the RED stack model from our research group (Tristán et al., 2020a), to find a middle ground between model fidelity and tractability. The semi-rigorous model is a system of differential and algebraic equations defining RED performance from cell pair to module scale. The reader is referred to (Tristán et al., 2020a) work and supplementary material for more details on the RED stack

Table 2
Upper and lower bounds on concentration of superstructure's streams.

Bounds	$sol = HC$	$sol = LC$
C^U_{sol}	$\max_{i \in S_{fsi} \subseteq S_i} (C_{i,HC})$	$C^U_{M,r}$
C^L_{sol}	$C^L_{M,r}$	$\min_{i \in S_{fsi} \subseteq S_i} (C_{i,LC})$

model.

As nonlinear optimization solvers are unable to handle integrals or differential equations directly, we reformulate first-order ordinary differential equations and integrals into algebraic equations, discretizing the x-domain with the backward finite difference method (implicit or backward Euler difference method) and applying the trapezoid rule, respectively (Butcher, 2016; Nicholson et al., 2017).

When the RED unit is active (Y_r = True), the discretized model ($h_r(x) \leq 0$) in (34) computes the net power output, NP_r, that is added to the nameplate generating capacity of the RED system, i.e., the total net power output, *TNP* in Eq. (21); otherwise ($\neg Y_r$), the net power output and cost terms in the objective function are set to zero.

3.4. Flow and mass balances formulation

We formulate flow and mass balance equations considering total flows (volumetric flow rate, Q in $m^3 \cdot h^{-1}$) and species composition (molar concentration of sodium chloride, C in $mol \cdot m^{-3}$) Karuppiah and Grossmann, 2006; Quesada and Grossmann, 1995), of the high- and low-salinity streams. The general mass balances in ((2) and (3) are in both the global constraints (e.g., applied to the feed, discharge units in the overall flowsheet, and source and sink child units in RPU parent block) as well as in $r_r(x) \leq 0$ constraints when the RED unit is active.

The mixer balances (2) apply to the inlet ports of the discharge units, the sink units, and the active RED units (i.e., when Y_r = True); mixing equations are nonlinear and nonconvex due to bilinear terms from the product of volumetric flows times molar concentration, which makes it difficult to find the global optimum.

$$\begin{aligned} Q_{k,sol}\ C_{k,sol} &= \sum_{i \in S_i \subseteq S} Q_{i,sol}\ C_{i,sol}, \\ Q_{k,sol} &= \sum_{i \in S_i \subseteq S} Q_{i,sol}, \\ &\forall\ \text{sol} \in SOL,\ k \in S_k \subseteq S \end{aligned} \tag{2}$$

The linear splitter balances (3) apply to the outlet ports of the feed units, the source units, and the active RED units (i.e., when Y_r = True).

$$\begin{aligned} C_{i,sol} &= C_{k,sol}, \\ Q_{i,sol} &= \sum_{k \in\ S_k \subseteq S} Q_{k,sol}, \\ &\forall\ sol \in SOL,\ i \in S_i \subseteq S \end{aligned} \tag{3}$$

For the set of candidate RED units, the index k in splitting Eqs. (3) is *(r,ro)* corresponding to the exhausted streams from RED's compartments leaving the high salinity and low salinity outlet ports. In the mixing equations (2), the index *i* refers to the streams flowing from the inlet port to the RED unit's compartments *(ri,r)*. The remainder index notations are summarized in Table 1.

3.5. Bounds on variables

Using (4) and (5), we calculate the value, and upper (superscript U) and lower (superscript L) bounds of candidate RED units' flowrate (i.e., streams $s \in S_r \subseteq S$) in (6). Each RED unit has upper limits on the flowrate, according to the maximum linear crossflow velocity ($m \cdot s^{-1}$), v^U_r, along the channel's length of the RED stack as the manufacturer specifies (Table 3). The lower bound v^L_r is a designer specification. In (4) and (5), $v_{r,sol}$ is the average linear crossflow velocity along RED units' channel length. The product $N_{cp}\ \varepsilon_{sp,sol}\ b\ \delta_{sp,sol}$ in (5) yields the cross-sectional area, A_r (m^2), of all RED unit's compartments, where N_{cp} is the number of cell pairs, $\varepsilon_{sp,sol}$ (-) the porosity, b (m) the width, and $\delta_{sp,sol}$ (m) the thickness of the concentrate and diluate spacers, which are parameters of the RED stack model (see Table 3).

$$v^L_r \leq v_{r,sol} \leq v^U_r \quad \forall\ sol \in SOL,\ r \in RU \tag{4}$$

$$\begin{aligned} Q_{s,sol} &= v_{r,sol} \left(N_{cp}\ \varepsilon_{sp,sol}\ b\ \delta_{sp,sol}\right)_r \\ &= v_{r,sol}\ A_r \\ &\forall\ sol \in SOL,\ s \in S_r,\ r \in RU \end{aligned} \tag{5}$$

$$\begin{aligned} &Q^L_{r,sol} \leq\ Q_{s,sol} \leq\ Q^U_{r,sol} \\ &\forall\ sol \in SOL,\ s \in S_r,\ r \in RU \end{aligned} \tag{6}$$

The subset of streams $s \in S \setminus S_r$ have upper bounds on flowrate (7), as given in (8) for outlet and inlet ports of the sink and source units, respectively (i.e., streams $s^{\in} S_{rmo} \cup S_{rsi}$), while for the inlet and outlet ports (i.e., streams $s^{\in} S_{rmi} \cup S_{rso}$) (9) applies.

$$0 \leq Q_{s,sol} \leq\ Q^U_{s,sol} \quad \forall\ sol \in SOL \tag{7}$$

$$\begin{aligned} Q^U_{s,sol} = &\begin{cases} v^U_r\ A_r,\ Q^U_{r,sol} \leq \sum_{i \in S_{fsi} \subseteq S_i} Q_{i,sol} \\ \sum_{i \in S_{fsi} \subseteq S_i} Q_{i,sol},\ Q^U_{r,sol} > \sum_{i \in S_{fsi} \subseteq S_i} Q_{i,sol} \end{cases} \\ &\forall\ sol \in SOL,\ s^{\in} S_{rmo} \cup S_{rsi},\ r \in RU \end{aligned} \tag{8}$$

$$\begin{aligned} Q^U_{s,sol} = &\begin{cases} N_r\ v^U_r\ A_r,\ Q^U_{r,sol}\ N_r \leq \sum_{i \in S_{fsi} \subseteq S_i} Q_{i,sol} \\ \sum_{i \in S_{fsi} \subseteq S_i} Q_{i,sol},\ Q^U_{r,sol}\ N_r > \sum_{i \in S_{fsi} \subseteq S_i} Q_{i,sol} \end{cases} \\ &\forall\ sol \in SOL,\ s^{\in} S_{rmi} \cup S_{rso},\ r \in RU \end{aligned} \tag{9}$$

We use (10)–(12) to define the upper and lower limits on the concentrate and diluate streams' molar concentration (Table 2).

$$\begin{aligned} \phi^U_r &= \frac{Q^U_{r,LC}}{Q^L_{r,HC} + Q^U_{r,LC}} \\ \phi^L_r &= \frac{Q^L_{r,LC}}{Q^U_{r,HC} + Q^L_{r,LC}} \end{aligned} \quad \forall r \in RU \tag{10}$$

where ϕ (-) is the ratio of diluate solution's flowrate to the total flowrate that is fed to the RED unit.

$$\begin{aligned} C^U_{M,r} &= \phi^L_r \max_{i \in S_{fsi} \subseteq S_i} (C_{i,LC}) + (1 - \phi^L_r) \max_{i \in S_{fsi} \subseteq S_i} (C_{i,HC}), \\ C^L_{M,r} &= \phi^U_r \min_{i \in S_{fsi} \subseteq S_i} (C_{i,LC}) + (1 - \phi^U_r) \min_{i \in S_{fsi} \subseteq S_i} (C_{i,HC}), \\ &\forall r \in RU \end{aligned} \tag{11}$$

$C_{M,r}$ ($mol \cdot m^{-3}$) is the concentration of the mixed solution reaching equilibrium.

$$C^L_{sol} \leq C_{s,sol} \leq C^U_{sol} \quad \forall\ sol \in SOL,\ s \in S \tag{12}$$

The high salinity streams' concentration could be as high as the maximum concentration of the feed streams, *in* (if there are multiple feed alternatives), while for the low salinity streams, the molar concentration could be as high as the concentration reached after the complete mixing of the concentrate and diluate stream (if reached thermodynamic equilibrium). The opposite holds for the lower bound on the concentration of the concentrate and diluate streams.

3.6. Boundary conditions and linking constraints

When the RED unit is active (Y_r = True), the boundary conditions

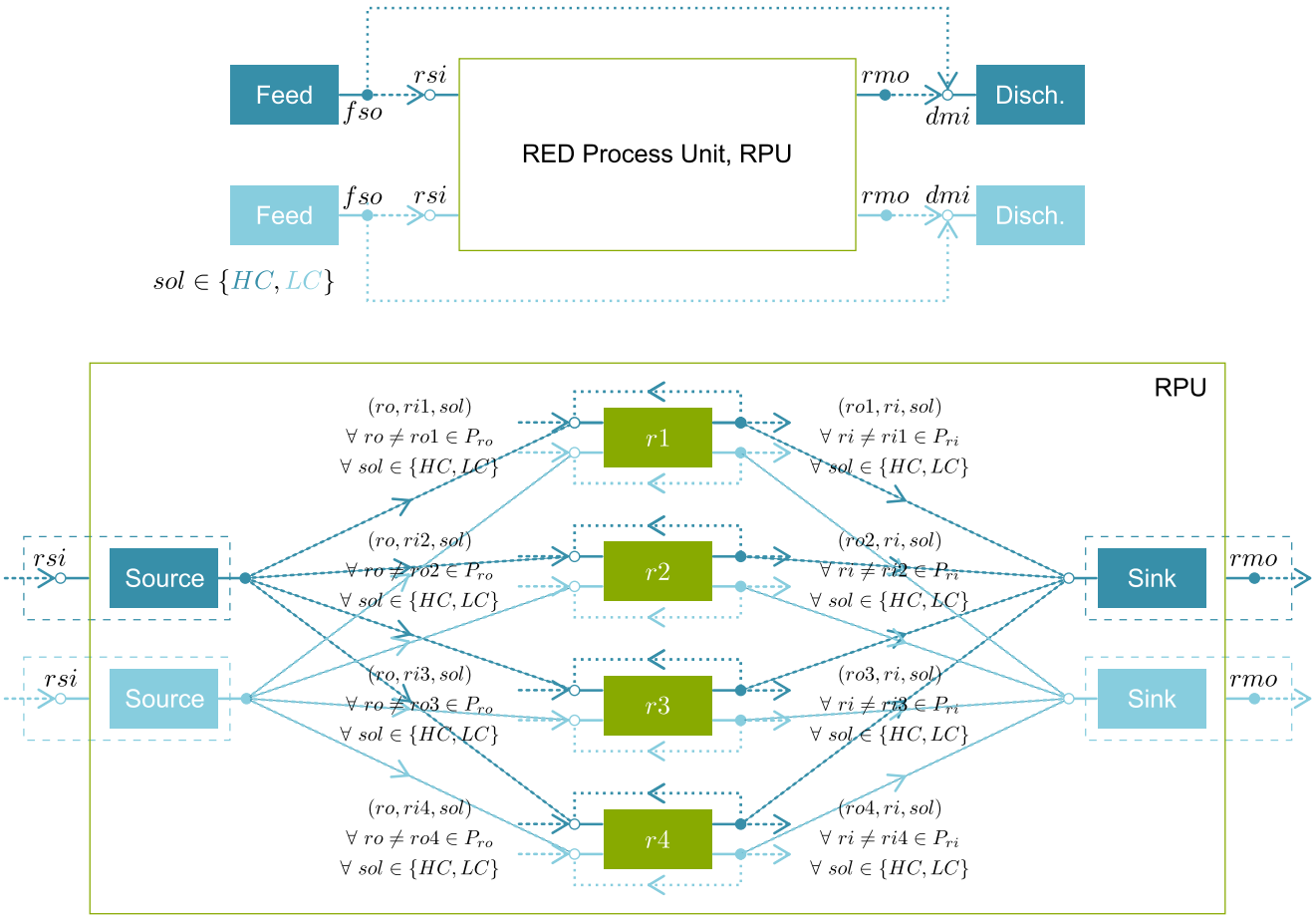

Fig. 4. RED process superstructure with four conditional RED units. In the bottom graph, the parent RED Process Unit, RPU, embeds the set of candidate RED units, $r \in RU$, a pair of source, $rs \in RSU$, and sink, $rm \in RMU$, permanent units for the high-salinity, *HC*, and low-salinity, *LC*, streams.

(13) link the inlet port *ri* with the RED unit's inlet compartments (i.e., $x_r = 0$), and (14) the outlet from the set of cell pairs (i.e., $x_r = L$) with the outlet port *ro* of the RED unit.

$$\begin{aligned} C_{ri,r,sol} &= C_{0,r,sol}, \\ Q_{ri,r,sol} &= N_{cp}\, Q_{0,r,sol}, \end{aligned} \qquad \forall\, sol \in SOL,\ r \in RU,\ ri \in P_{ri} \subseteq P_{in} \tag{13}$$

$$\begin{aligned} C_{r,ro,sol} &= C_{L,r,sol}, \\ Q_{r,ro,sol} &= N_{cp}\, Q_{L,r,sol}, \end{aligned} \qquad \forall\, sol \in SOL, r \in RU,\ ro \in P_{ro} \subseteq P_{out} \tag{14}$$

When the RED unit is absent ($\neg Y_r$) (15) applies.

$$\begin{aligned} C_{s,sol} &= C^L_{sol} \quad \forall\, s \in S_{ri} \cup S_{ro}, \\ \sum_{i \in S_{ri} \subseteq S_i} Q_{i,sol} &= 0, \\ Q_{rso,ri,sol} &= 0 \quad \forall\, rso \in P_{rso},\ ri \in P_{ri}, \\ &\qquad \forall\, sol \in SOL \end{aligned} \tag{15}$$

3.7. Logic constraints

We add the following logic propositions:

(a) A programming logic constraint (16) enforcing that at least one *RU* is active in the RPU section:

$$\sum_{r=1}^{N_r} Y_r \tag{16}$$

(b) Since all candidate RED units are equal, we added symmetry-breaking constraints (17) to avoid structural redundancy (combinatorial redundancy) by eliminating symmetric solutions, thus, easing the computational effort.

$$Y_{r+1} \Rightarrow Y_r \quad \forall\, r \in RU \tag{17}$$

3.8. Objective function: maximize the net present value (NPV)

The objective of the GDP problem is to maximize the *NPV* of the RED process. The *NPV* (18) considers operating (*OPEX* in $USD_{2019}{\cdot}year^{-1}$), and capital costs (*CAPEX* in USD_{2019}) annualized over the expected lifetime of the plant, *LT* in years (Table 4). The *CAPEX* is annualized using the capital recovery factor (*CRF*) given in (20) with an interest rate *r* (Table 4). The annualized *CAPEX* and *OPEX* define the total annual cost (19), *TAC*, of the RED system. The *NPV* accounts for profits from RED's electricity sales. We assume the surplus electricity unexpended by the RED plant is sold to the grid at EU-27 2019-average price of electricity for non-house consumers (Band IB: annual consumption between 20 and 500 MWh excluding taxes and levies), i.e., $ep = 0.11$ €·kWh^{-1} ($0.12 kWh^{-1}).

Table 3
Parameters of the commercial RED stack (Fumatech GmbH®, Germany).

Parameter	Value
Maximum flow velocity, v_r^U (cm·s^{-1})	3.0
Number of cell pairs, N_{cp} (-)	1000
Channel size, b (m) × L (m)	0.456 × 0.383
Spacers	
Thickness, δ_{sp} (μm)	270[a]
Porosity, ε_{sp} (-)	82.5%
Membranes properties: fumasep® CEM (FKS-50) / AEM (FAS-50)	
Areal resistance, R_{IEM0} (Ω·cm^2)	1.8 / 0.6[b]
Permselectivity, α_{IEM0} (-)	0.93
Thickness dry, δ_{IEM} (μm)	50
Active area, $b \times L$ (m^2)	0.175

[a] Equal to inter-membrane distance i.e. height of the HC or the LC channels.
[b] Measured in 0.5 M NaCl at 25 °C.

Table 4
Financial parameters for the RED plant.

Parameter	Value
Plant lifetime, *LT* (years)	20
Membranes' lifetime, LT_m (years)	2
Load Factor, *LF*	90%
Discount rate, *r* (IRENA, 2022)	7.5%

$$NPV = \frac{ep\ TNP\ 8760\ LF - TAC}{CRF} \tag{18}$$

$$TAC = CRF\ CAPEX + OPEX \tag{19}$$

$$CRF = \frac{r}{1 - (1 + r)^{-LT}} \tag{20}$$

$$TNP = \sum_{r \in RU} NP_r \tag{21}$$

The annual energy yield (kWh·$year^{-1}$) of the RED plant working at full capacity, i.e., 8760 full load hours per year, is corrected with a load factor, *LF*, of 90% (i.e., RED works 8000 h each year) to account for expected plant downtime due to membrane cleaning and system maintenance. The summation of the net power output over the candidate RED units yields the nominal capacity of the RED system (21) i.e., the total net power output, *TNP*, in kW.

To estimate the capital investment, we determine the cost of RED stacks, pumps, and civil and electrical infrastructure cost.

$$CAPEX = \sum_{r \in RU} CC_{stack,r} + CC_{pump} + CC_{civil} \tag{22}$$

The RED unit's cost, $CC_{stack,r}$ involves the cost of membranes, $CC_{IEMs,r}$, i.e., total membrane area, $2\ (N_{cp}\ b\ L)_r$, times the specific price of

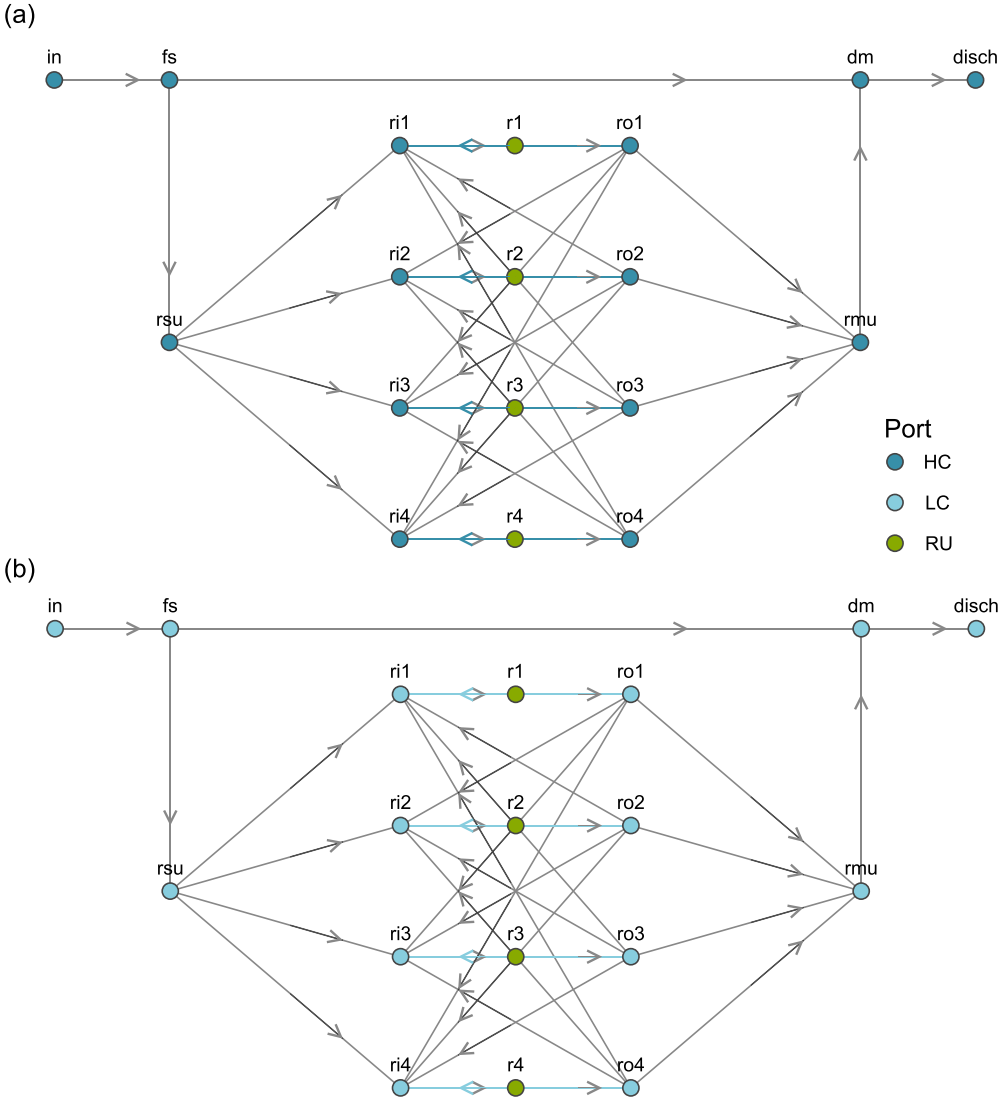

Fig. 5. Port representation of the RED process superstructure of alternatives in Fig. 4. The top graph (a) shows all feasible links between HC ports and the bottom graph (b) between LC ports. The dark and light blue-colored arrows represent the RED units' HC and LC recycled streams. Port notation: HC (high concentration ports), LC (low concentration ports), and RU (RED units' HC and LC ports). For ease of representation, the inlet and outlet ports of the feed, source, sink, and discharge units are lumped into ports fs, rsu, rmu, and dm.

Table 5
Specifications of the illustrative example and the cases of study.

	Candidate RED units, *Nr*	LC Concentration (mM)	Flowrate ($m^3 \cdot h^{-1}$)	
			HC	LC
Example	4	4	10	10
Case study				
Scenario #1	10	4	100	100
Scenario #2	10	40	10	10

Membrane's price is 2.0 $€ \cdot m^{-2}$. HC feed concentration = 1.23 M NaCl. $T = 25$ °C.

membranes, *cm*, and the cost of electrodes and stack, which is assumed to be 51.7% of the current membrane cost (Papapetrou et al., 2019). When the RED unit is absent, the capital cost of the stack is set to zero.

$$\begin{aligned} CC_{stack,r} &= CC_{IEMs,r}\ (1\ +\ 0.517) \\ &= 2\ cm\ \left(N_{cp}\ b\ L\right)_r (1\ +\ 0.517) \end{aligned} \tag{23}$$

We estimate the concentrate and diluate pump costs, CC_{pump}, using Sinnot and Towler's (Sinnott and Towler, 2020) non-linear correlation as given in (24), valid between 0.2 and 126 $L \cdot s^{-1}$ (0.72–453.6 $m^3 \cdot h^{-1}$). The purchased pump's cost on a U.S. Gulf Coast basis, Jan. 2007 is converted to 2019 dollars with the Chemical Engineering Plant Cost Index (CEPCI).

$$CC_{pump} = \frac{CEPCI_{2019}}{CEPCI_{ref}} \sum_{sol \in SOL} \left[a + b \left(\sum_{k \in S_{rso} \subseteq S_k} Q_{k,sol} \right)^{\beta} \right] \tag{24}$$

$$CC_{pump} = \frac{CEPCI_{2019}}{CEPCI_{ref}} \sum_{sol \in SOL} \left[a + b\ Z_{sol} \right] \tag{25}$$

$$Z_{sol} = \left(\sum_{k \in S_{rso} \subseteq S_k} Q_{k,sol} \right)^{\beta} \tag{26}$$

$$Z_{sol} \geq \left(\sum_{k \in S_{rso} \subseteq S_k} Q_{k,sol} \right)^{\beta} \tag{27}$$

$$\sum_{k \in S_{rso} \subseteq S_k} Q_{k,sol} - Z_{sol}^{1/\beta} \leq 0 \tag{28}$$

where a, b, and β are cost parameters and the sizing variable is the flowrate of streams leaving the source units in the RPU given in $L \cdot s^{-1}$.

Power law expressions whose exponent is lower than one, such as pumps' investment cost, are concave and, as such, a source of computational difficulties due to unbound derivatives when the flows (the sizing variable) take zero values (Cafaro and Grossmann, 2014).

A common workaround to bound gradients for zero flows is to add a small tolerance to the sizing variable in the concave cost function

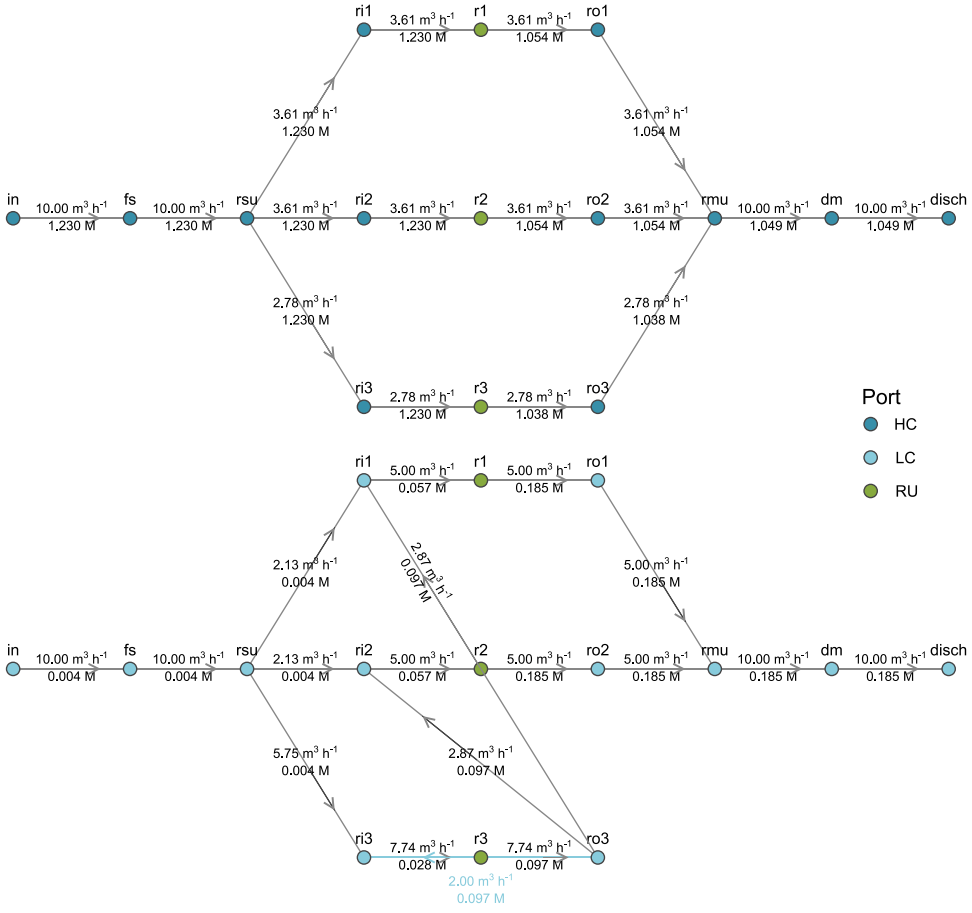

Fig. 6. Illustrative example result: Port representation of the NPV-optimal RED process design with three active RED units. The top graph shows the links between HC ports and the bottom graph between LC ports.

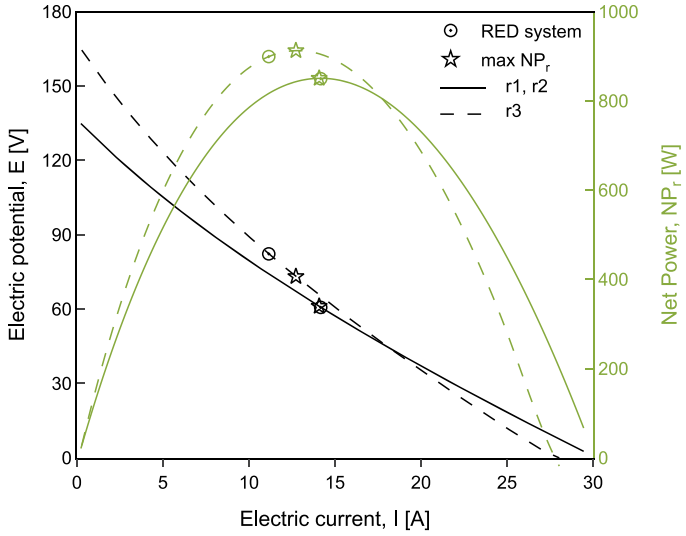

Fig. 7. Illustrative example results: Polarization and power curves of the active RED units r1, r2, and r3. Markers denote the maximum net-power working conditions (max NP_r) and the NPV-optimal RED process working conditions (RED system) of the RED units.

(Ahmetović and Grossmann, 2011). Even though smaller tolerances provide better approximations of the original cost function, they also yield larger derivatives when flows are zero due to ill-conditioning for the NLP. Hence, to prevent this numerical issue, we propose to reformulate the concave pump cost term (24) into a linear function (25), adding a new variable Z_{sol}, defined in (26), to replace the size variable raised to the β^{th} and rearranged into inequality (27) since it is guaranteed to be active due to the monotonicity of Z_{sol} in the cost function (25) (Grossmann, 2021; Papalambros and Wilde, 2018). The inequality (27) is rearranged into inequality (28) by raising the left- and right-hand sides to the power $1/\beta$. Note that $Z_{sol}^{1/\beta}$ in (28) has a bounded derivative ($\partial Z_{sol}^{1/\beta}/\partial Z = Z^{1/\beta-1}/\beta$) at $Z_{sol} = 0$ since $1/\beta - 1 > 0$. The inequality (28) is still nonconvex, but it avoids the problem of unbounded derivative for zero values in the variable $Q_{k,sol}$.

We compute the civil and electrical infrastructure costs as follows:

$$CC_{civil} = ccivil\ TNP \tag{29}$$

where *ccivil* is the cost parameter (250 €·kW^{-1}) (Papapetrou et al., 2019).

The annual operating cost comprises the electricity consumption cost of pumps, $OC_{pump,r}$, the replacement cost of membranes, $OC_{IEMsrep,r}$, and maintenance and labor costs (as 2% of CAPEX).

$$OPEX = \sum_{r\in RU} OC_{pump,r} + \sum_{r\in RU} OC_{IEMsrep,r} + 0.02\ CAPEX \tag{30}$$

When the RED unit is active, (31) and (32) are enforced, if not $OC_{pump,r}$ and $OC_{IEMsrep,r}$ are set to zero.

In (31), *ep* (USD$_{2019}$·kWh^{-1}) is the electricity price, and PP_r in kW, the power consumed to overcome the pressure drop in the high- and low-concentrated channels of the RED unit.

$$OC_{pump,r} = ep\ LF\ 8760\ PP_r \tag{31}$$

To estimate the replacement cost of membranes (32), we convert the series of disbursements at the end of the lifetime of membranes, LT_m (Table 4), into an equivalent yearly annuity considering the first payment as a future value over the first period (i.e., LT_m) and finding the equivalent annuity over that period using the sinking fund factor. The sinking fund factor converts a single future amount, i.e., CC_{IEMs}, into a series of equal-sized disbursements, $OC_{IEMsrep,r}$, made over LT_m equally spaced intervals, at the given interest rate r compounded annually (Fraser and Jewkes, 2012).

$$OC_{IEMsrep,r} = CC_{IEMs}\frac{r}{(1+r)^{LT_m} - 1} \tag{32}$$

Wherever needed, all currencies were converted to USD$_{2019}$ according to the historical average exchange rate of the corresponding publication year.

3.9. Economic performance metrics: levelized cost of energy (LCOE)

The LCOE (USD$_{2019}$ kWh^{-1}), a common metric to benchmark different renewable power technologies, estimates the average cost per unit of energy generated across the lifetime of a power plant that would break even the RED project costs. The LCOE gives a first-order assessment of 1he RED project viability (Krey et al., 2014).

Assuming the energy provided annually is constant during the lifetime of the project, the LCOE reduces to (33).

$$LCOE = \frac{CRF\ CAPEX + OPEX}{TNP\ 8760\ LF} \tag{33}$$

The set of Eq. (34) shows the explicit representation of the GDP model (1) with *Nr* explicit disjunctions to decide whether the RED units exist or not.

$$
\begin{aligned}
\max NPV = \; & f(x) \\
s.t. \; & \left.\begin{aligned} Q_{k,sol}\, C_{k,sol} &= \sum_{i \in S_{rmi} \cup S_{dmi} \subseteq S_i} Q_{i,sol}\, C_{i,sol}, \\ Q_{k,sol} &= \sum_{i \in S_{rmi} \cup S_{dmi} \subseteq S_i} Q_{i,sol} \end{aligned}\right\} \forall\, sol \in SOL, k \in S_{rmo} \cup S_{dmo} \subseteq S_k \\
& \left.\begin{aligned} C_{i,sol} &= C_{k,sol}\ \forall\, k \in S_{fso} \cup S_{rso} \subseteq S_k, \\ Q_{i,sol} &= \sum_{k \in S_{fso} \cup S_{rso} \subseteq S_k} Q_{k,sol} \end{aligned}\right\} \forall\, sol \in SOL, i \in S_{fsi} \cup S_{rsi} \subseteq S_i \\
& \left[\begin{array}{c} Y_r \\ \textbf{\textit{RED stack model equations}}: \\ h_r(x) \le 0 \\ \textbf{\textit{Inlet port (mixer) balances}}: \\ \left.\begin{aligned} Q_{k,sol}\, C_{k,sol} &= \sum_{i \in (ri,r) \subseteq S_i} Q_{i,sol}\, C_{i,sol}, \\ Q_{k,sol} &= \sum_{i \in (ri,r) \subseteq S_i} Q_{i,sol} \end{aligned}\right\} \\ \forall\, sol \in SOL, k \in (r, ro) \subseteq S_k \\ \textbf{\textit{Outlet port (splitter) balances}}: \\ \left.\begin{aligned} C_{i,sol} &= C_{k,sol}\ \forall\, k \in (r, ro) \subseteq S_k, \\ Q_{i,sol} &= \sum_{k \in (r,ro) \subseteq S_k} Q_{k,sol} \end{aligned}\right\} \\ \forall\, sol \in SOL, i \in (ri, r) \subseteq S_i \\ \textbf{\textit{Bounds on flowrate of streams}}: \\ \left.\begin{aligned} v_r^L &\le v_{r,sol} \le v_r^U, \\ Q_{s,sol} &= v_{r,sol}\, A_r, \\ Q_{r,sol}^L &\le Q_{s,sol} \le Q_{r,sol}^U \end{aligned}\right\} \forall\, s \in S_r, \\ \forall\, sol \in SOL, r \in RU \\ \textbf{\textit{Bounds on concentration of streams}}: \\ C_{sol}^L \le C_{s,sol} \le C_{sol}^U\ \forall\, sol \in SOL, s \in S_r, \\ C_{sol}^U \text{ and } C_{sol}^L \text{ in Table 2} \\ \textbf{\textit{Boundary conditions and linking constraints}}: \\ \textit{From inlet port to RED unit compartments } (x_r = 0) \\ \left.\begin{aligned} C_{ri,r,sol} &= C_{0,r,sol}, \\ Q_{ri,r,sol} &= N_{cp}\, Q_{0,r,sol} \end{aligned}\right\} \forall\, sol \in SOL, r \in RU, ri \in P_{ri} \subseteq P_{in} \\ \textit{From RED unit compartments } (x_r = L) \textit{ to outlet port} \\ \left.\begin{aligned} C_{r,ro,sol} &= C_{L,r,sol}, \\ Q_{r,ro,sol} &= N_{cp}\, Q_{L,r,sol} \end{aligned}\right\} \forall\, sol \in SOL, r \in RU, ro \in P_{ro} \subseteq P_{out} \\ \textbf{\textit{RED stack capital investment}}: \\ CC_{stack,r} = CC_{IEMs}\,(1 + 0.517) \\ \textbf{\textit{Pumps and membranes' replacement operating costs}}: \\ OC_{pump,r} = ep\, LF\, 8760\, PP_r \\ OC_{IEMsrep,r} = CC_{IEMs} \dfrac{r}{(1+r)^{LT_m} - 1} \end{array}\right] \veebar \left[\begin{array}{c} \neg Y_r \\ NP_r = 0 \\ \left.\begin{aligned} C_{s,sol} &= C_{sol}^L\ \forall\, s \in S_{ri} \cup S_{ro}, \\ \sum_{i \in S_{ri} \subseteq S_i} Q_{i,sol} &= 0, \\ Q_{s,sol} &= 0\ \forall\, s \in (rso, ri) \subseteq S_{ri} \cup S_{rso} \end{aligned}\right\} \forall\, r \in RU \\ \forall\, sol \in SOL \\ CC_{stack,r} = 0 \\ OC_{pump,r} = 0 \\ OC_{IEMsrep,r} = 0 \end{array}\right] \qquad (34) \\
& 0 \le Q_{s,sol} \le Q_{s,sol}^U\ \forall\, sol \in SOL, s \in S\, S_r \\
& C_{sol}^L \le C_{s,sol} \le C_{sol}^U\ \forall\, sol \in SOL, s \in S\, S_r \\
& \Omega(Y_r) = True \\
& x \in X \subseteq R^n \\
& Y_r = \{True, False\}\ \forall\, r \in RU
\end{aligned}
$$

4. Illustrative example

We illustrate the functionality of the RED process optimization model using the superstructure in Fig. 4, with four conditional industrial-scale RED stacks (relevant parameters in Table 3). An actual RED plant will probably house several hundred RED units, especially as regards economies-of-scale cost reduction. But we decide to stick to four RED units to provide an illustrative demonstration of the GDP model. The same logic applies to feeds volume; to represent a low-availability feed case, we set the volume of the HC and LC feeds roughly equal to the maximum inlet flowrate of the RED units (i.e., $Q_{fso,\ rsi,sol} \cong Q_{r,sol}^U\ \forall\ sol \in SOL$). Later, in the Case Study, we assess the influence of the feeds availability on the optimal design of the RED process. The size and computational performance of the GDP model can

be found in Section 6. For ease of representation, Fig. 5 shows a split view of the high salinity (top graph, a) and low salinity (bottom graph, b) units' ports and all feasible streams of the RED process superstructure in Fig. 4. For the given high- and low-salinity feed streams' properties (i.e., flow velocity, concentration, and temperature), and membranes cost in Table 5, and the given parameters (Tables 3 and 4), the solution of the GDP problem in Eqs. (1)–(34) provides the cost-optimal NPV topology, shown in Fig. 6, and decision variables that balance electricity production and the increase in capital and operating expenses. Discrete decisions involve the working RED units and the active water streams. Continuous decisions are the flowrate and concentration of the inlet streams and the electric current of each active RED stack. We set the volume of the HC and LC feeds roughly equal to the maximum inlet flowrate of the RED units (i.e., $Q_{fso,\ rsi,sol} \cong Q^{U}_{r,sol}\ \forall\ sol \in SOL$).

To assess the optimal solution to the GDP problem, we also estimate the working conditions (i.e., the concentration of the low-salinity inlet stream, the flowrate of the high and low-salinity inlet streams, and the electric current) that maximize the net power output of the stand-alone RED stack.

The NPV-optimal solution, whose port representation is in Fig. 6, keeps three RED units working. The limited number of active RED units restricts the nominal capacity of the RED system (2.60 kW), as such, the capital and operational expenses outweigh the benefits from electricity sales resulting in an unprofitable design (negative NPV of $15,391, and LCOE of $194 MWh^{-1} above electricity market price). Larger membranes' lifetimes, which it is acceptable given the mild working conditions of the RED units, and economies of scale would bring clear cost reductions that would make the RED process profitable (Daniilidis et al., 2014; Post et al., 2010).

Regarding the working conditions of the optimal solution, the HC and LC flow velocity of the RED units declines below the estimated net-power-optimal value of the stand-alone RED stack (953 W) owing to pumps' investment and electrical consumption costs. Lower velocity means longer residence time of the HC and LC streams in the RED unit compartments facilitating the ions' transfer from the high salinity side to the low salinity one. Hence, to keep the concentration gradient for longer along channels, the LC inlet stream concentration of all RED units should be lower than the net-power optimal value (i.e., 40 mM). The limited high- and low-salinity feeds, however, constrain the inlet flowrate of the RED units and so the chances to reach the optimal LC inlet concentration. Hence, the recycled and reused LC streams from RED unit r3 increase the LC inlet stream concentration of all RED units above the optimal value (Fig. 6).

The RED unit r3 works with a less saline LC inlet stream, a higher LC

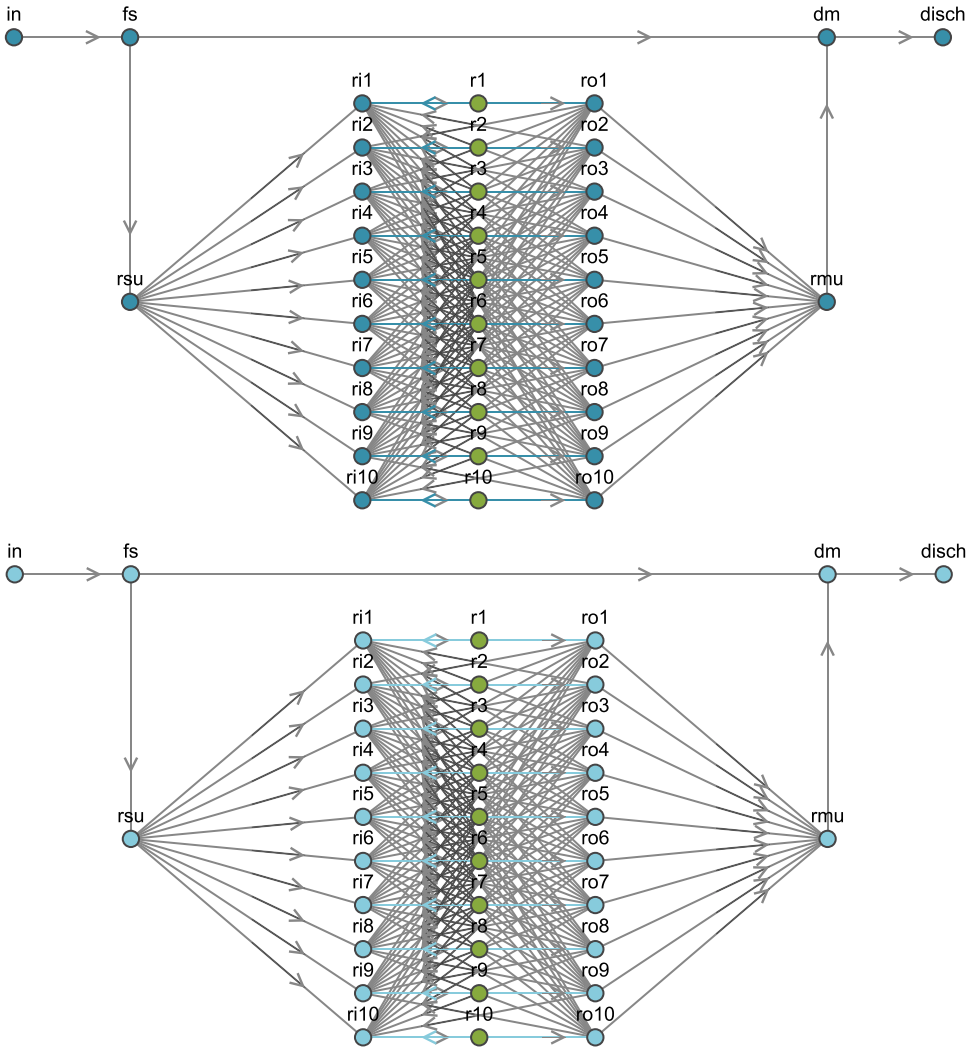

Fig. 8. Case Study. Port representation of the RED process superstructure with ten RED candidate units for scenarios #1 and #2. The top graph shows all feasible links between HC ports and the bottom graph between LC ports. The dark and light blue-colored arrows represent the RED units' HC and LC recycled streams. Port notation: HC (high concentration ports), LC (low concentration ports), and RU (RED units' ports).

flow, and a lower HC flow than the remainder active units such that the concentration of the LC inlet streams approaches the optimum once the r3's outlet LC streams mix with the 4 mM LC feed (Fig. 6). The RPU's source unit, rs, supplies a lower volume of HC than LC feed to the RED units, since higher flow velocities in LC than in HC compartments enhances the net power of the RED unit (Ortiz-Martínez et al., 2020; Tristán et al., 2020a).

The polarization and power curves of the RED units (Fig. 7) vary according to the inlet streams' flowrate and concentration, and so does the optimum working point. That is, the GDP model adjusts the electric current of each RED unit to peak its net power output except unit r3, whose electric current is reduced below the optimum to slow down the electromigration of ions across membranes. The reduced electromigrative transport thereby limits the LC stream concentration increase.

5. Case study

Once we have demonstrated the GDP model functionality in the illustrative example, we now apply the GDP optimization model to superstructure in Fig. 8, with ten industrial-scale RED candidate units (with the same parameters as the illustrative example, Table 3) and two feed scenarios (see Table 5) to explore the influence of the feedstreams concentration and availability on the cost-optimal topology and operating conditions of the RED process. In the high-availability case (scenario #1), we set the flowrates of the HC and LC feeds equal to the RED unit's maximum inlet flowrate times the number of candidate RED units in the superstructure ($Q_{fso,\ rsi,sol} \cong N_r\ Q^U_{r,sol}\ \forall\ sol \in SOL$). In the low-availability case (scenario #2), the volume of the HC and LC feeds are nearly equal to the maximum inlet flowrate of the RED units ($Q_{fso,\ rsi,sol} \cong Q^U_{r,sol}\ \forall\ sol \in SOL$). We discuss the model size and computational performance of the two cases of study in Section 6. As in the illustrative example, we compare the working conditions of each RED stack in the cost-optimal design with those that would maximize the net power of the stand-alone RED unit. To size the improvement in cost-competitiveness of the RED process, we also compare the optimal configuration in scenarios #1 and #2 with a series arrangement of the RED units without either recycling or reusing alternatives of the RED units' outlet streams, and the same number of candidate units. To reproduce the series layout from our previous assessment (Tristán et al., 2020b), we fix the net-power optimal concentration and flow velocities of the stand-alone RED unit to the inlet feedstreams of the series, the electric current of each RED unit is left as a decision variable and is adjusted to maximize the net power of the RED system.

The GDP optimization model predicts the NPV-optimal flowsheet design from the representation of alternatives, whose port representation is in Fig. 8, for the given: (i) high- and low-salinity feed availability (i.e., ~100 and ~10 $m^3 \cdot h^{-1}$) and (ii) low-salinity feed concentration (i.e., 40 and 4 mM NaCl) in scenarios #1 and #2.

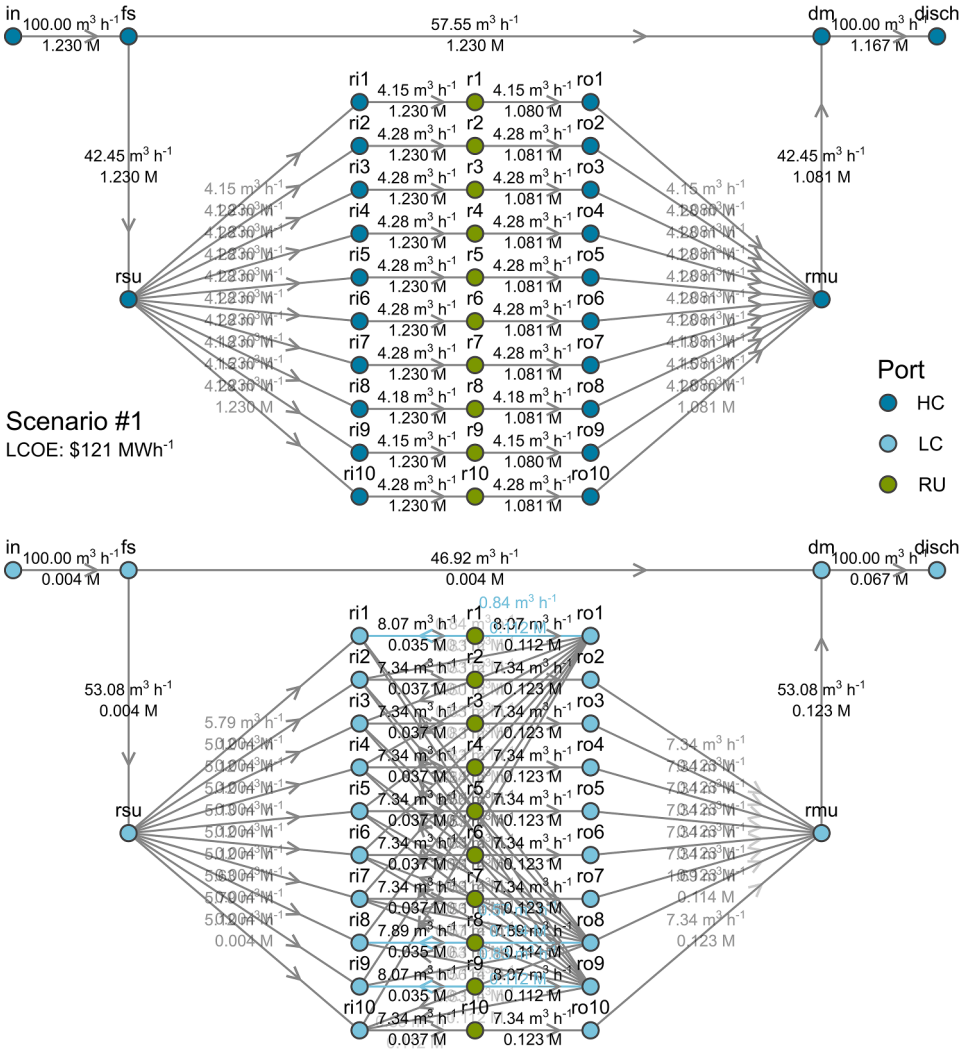

Fig. 9. Port representation of the optimal RED system design for feed scenario #1. The top graph shows the links between HC ports and the bottom graph between LC ports.

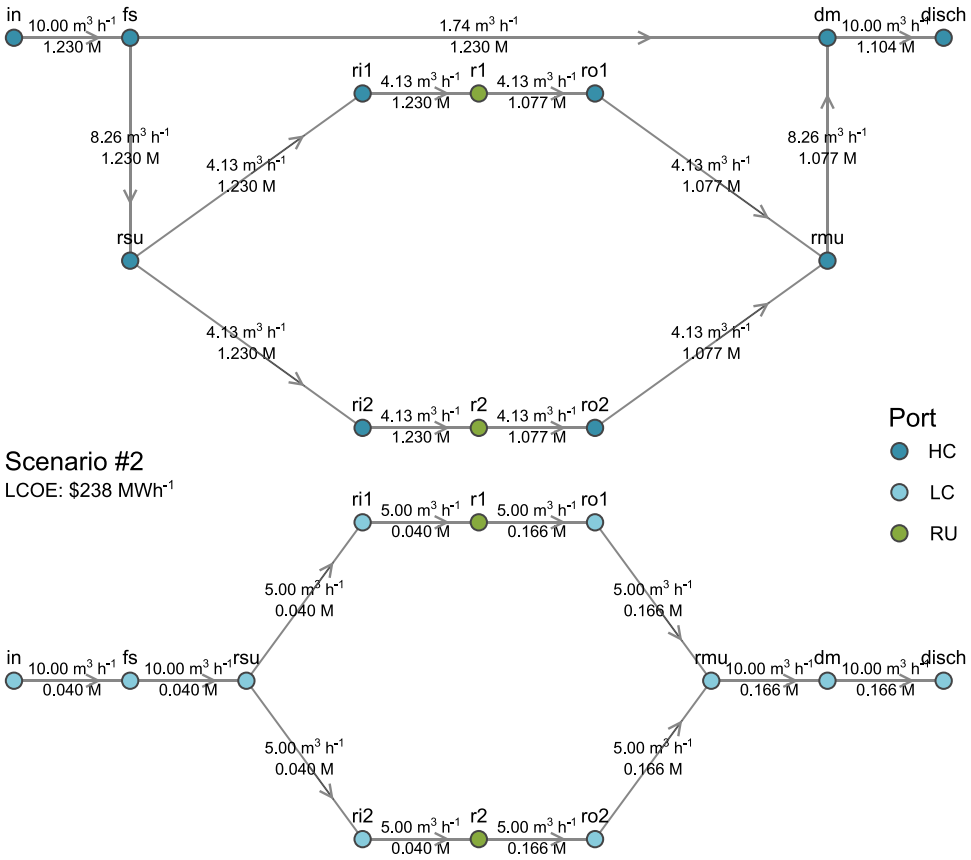

Fig. 10. Port representation of the optimal RED system design for feed scenario #2. The top graph shows the links between HC ports and the bottom graph between LC ports.

Table 6
Case study optimal results: Techno-economic performance metrics of series layout, and scenarios #1 and #2.

	TNP (kW)	LCOE($·MWh-1)	NPV ($)
Series	3.65	293	−50,800
Scenario #1	9.35	121	−543
Scenario #2	1.78	238	−16,789

TNP: Total Net Power; LCOE: Levelized Cost of Energy; NPV: Net Present Value.

The cost-optimal flowsheet design in scenarios #1 (Fig. 9) and #2 (Fig. 10) outperforms the conventional series arrangement (Table 6), albeit the feed conditions and the limited numbers of RED units in scenarios #1 and #2 render unprofitable RED process designs. Maximizing the total net power output requires larger disbursements that outweigh the meager profits from electricity sales, even if the feed conditions are more favorable than in scenario #2.

Feed scenario #1 yields the RED process' optimal design in Fig. 9. The larger feedstreams' volume allows installing more RED units, and the 4 mM LC feed adds reuse and recycling alternatives to the decision space, enabling the active RED units to work closer to the optimal net power conditions of the stand-alone RED stack (Figs. 11 and 12). The increased number of RED units working in near-optimal conditions thereby enhances the RED system power rating to 9.35 kW. As a result, revenues almost break even the total cost of the RED process (i.e., the LCOE almost equals the electricity market price and the NPV gets closer to zero, see Table 6).

The capital and operational costs of pumps cause the RED units' HC and LC inlet flowrate (Fig. 12) to be lower than the one that would maximize the net power output of the RED stack. Hence, the RED unit would deplete the concentration gradient earlier unless the LC inlet stream concentration of all RED units is decreased below the net-power optimal value (i.e., below 40 mM) as the optimization model predicts; the recycled and reused low-salinity streams from RED units r1, r8, and r9 concentrate the LC inlet stream of all RED units to reach the optimal value (Figs. 9 and 12). The electric current of each RED unit maximizes the net power output according to the inlet flow and concentration (Fig. 11) as in the illustrative example.

Feed scenario #2, shown in Fig. 10, yields an optimal flowsheet design with larger LCOE and lower NPV than scenario #1. The LC feed's limited availability restricts, even more, the HC and LC inlet flowrate of the RED units for the sake of profitability. To maximize the NPV of the RED process, the number of active RED units should decrease from ten in scenario #1 to two, such that the RED units' working conditions fit better to the adverse feed conditions. The 40 mM LC feed dwindles recycling and reuse alternatives that would improve the RED process power rating. A 4 mM rather than a 40 mM LC feed, as in the illustrative example, would enable adding a RED unit which results in a costlier but more productive RED system that offsets the TAC increase. The rise in the net power production from 1.78 to 2.60 kW would make the revenues share of total annual costs increase from ~50% up to ~62%.

Overall, these results illustrate how the GDP optimization model can assist the RED process conceptual design in determining the cost-optimal one out of a complex process configuration and working decision space. The reader must recall that the present study serves to illustrate the functionality of the GDP optimization model on the conceptual design of the RED process rather than giving actual figures of the RED technology. The scale-up of the RED process's nameplate capacity to the MW order with more candidate RED units and longer membranes' lifetime would likely make the project profitable (Post et al., 2010). For

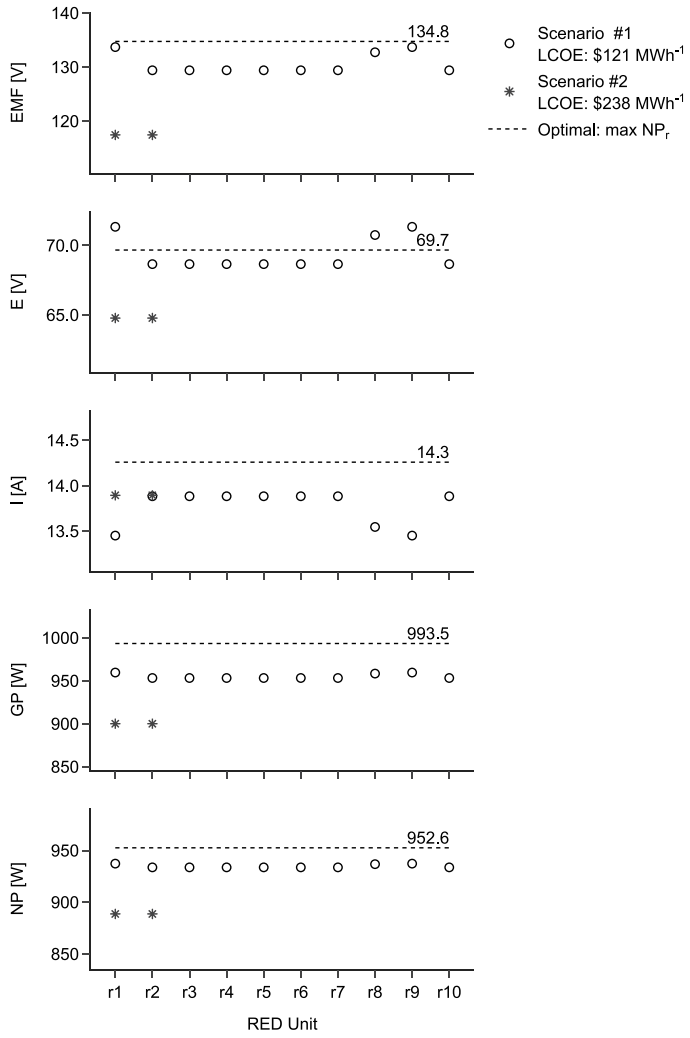

Fig. 11. Case Study results: NPV-optimal working conditions of the active RED units for scenarios #1 and #2, and the working conditions that maximize the net power output of the stand-alone RED stack. EMF: Electromotive force (Nernst potential); E: Electric potential of the stack; I: Electric current of the stack; GP: Gross power; NP: Net power.

instance, (Giacalone et al., 2019) estimated the LCOE of a large-scale RED plant recovering energy from several natural and anthropogenic SG sources. The authors assumed the high and low salinity feedwaters are equally split between a set of identical RED units arranged in parallel; the scarcer feed restricts the number of RED units that can be installed, and, accordingly, the nominal capacity of the RED plant. The RED plant sourced with SWRO brine (~1.2 M NaCl) and treated wastewater (17 mM NaCl)—akin to the Illustrative example and Case Study concentrations, but with far more feeds volume—would deliver two to three orders of magnitude more net power at a competitive cost. SGE-based technologies—yet in early development stages and, as such, costlier than other mature low-carbon power technologies—promise worthy benefits for society's welfare and environment protection and conservation. Hence, it is important to note that actual investment decisions must consider all these factors that LCOE and NPV, as they are defined, do not fully reflect. The GDP optimization model can incorporate sustainability criteria in the decision-making process through multi-objective optimization (MOO) coupled with life cycle assessment (LCA) principles (Guillén-Gosálbez et al., 2019; Kravanja and Čuček, 2013). The solution of a MOO provides a set of Pareto points representing the optimal trade-off between the conflicting environmental, social, and economic objectives (Guillén-Gosálbez et al., 2019). Alternatively, the GPD model can be economically, environmentally and socially wise using a single-objective economic function where the social and environmental impacts from LCA are converted into equivalent monetary units (i.e., monetizing the LCA results) (Pieragostini et al., 2012; Pizzol et al., 2015)

6. Computational results

Table 7 reports the GDP model sizes and solution times of the illustrative example with four candidate RED units, and the cases of study #1 and #2 with ten candidate RED units; scenarios #1 and #2 have equal sizes but different solution times subject to the feed streams conditions. We code and solve the GDP model with Pyomo algebraic modeling language written in Python (Hart et al., 2017) and Pyomo.GDP modeling environment for logic-based modeling and optimization (Chen et al., 2021a) on a machine running Windows 10 (x64) with 6 cores processor (Intel® Core™ i7–8700 CPU @3.2 GHz) and 16 GB of RAM.

We apply the Global Logic-based Outer Approximation (GLOA) algorithm (Chen et al., 2021a; Lee and Grossmann, 2001)—available in Pyomo.GDP through GDPopt solver—to solve the non-convex GDP problem (1)–(34). This strategy decomposes the solution to the GDP into reduced NLP subproblems and master MILP problems, to avoid "zero-flow" numerical issues arising in nonlinear design problems when units or streams disappear.

The MILP master problem is solved with CPLEX and the reduced NLP subproblems with the multistart heuristic algorithm MSNLP and

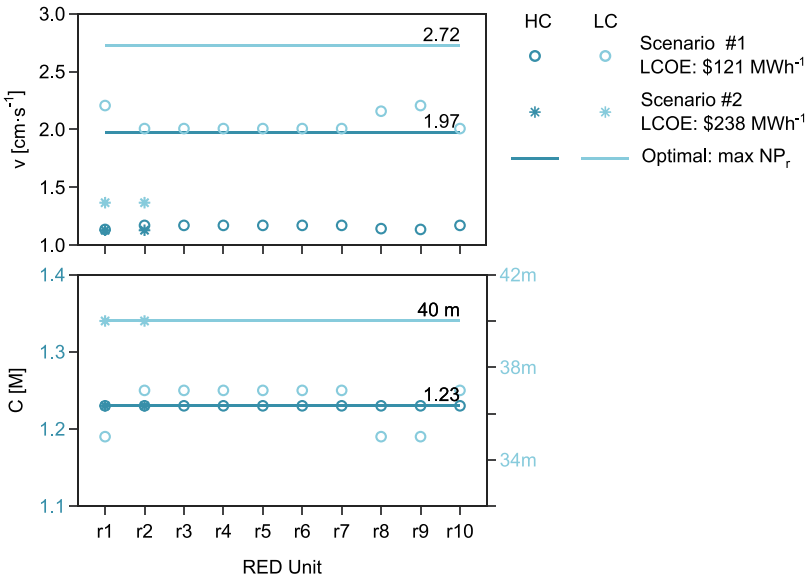

Fig. 12. Case Study results: NPV-optimal inlet linear velocity and molar concentration of the active RED units for scenarios #1 and #2, and the working conditions that maximize the net power output of the stand-alone RED stack. v: linear crossflow velocity within the RED unit's channel; C: NaCl molar concentration of the RED unit's inlet stream.

Table 7
GDP model size, solution time, and objective function value for the illustrative example and the cases of study.

		vars	Bool	cont	cons (nl)	disjtn	CPU Time (s)	NPV ($)
Example		1226	8	1218	1298 (278)	4	35	−15,348
Case study	#1	3278	20	3258	3458 (686)	10	282	−543
	#2						328	−16,789

Headings: vars = variables, Bool = Boolean variables, cont = continuous variables, cons = constraints, nl = nonlinear constraints, disjtn = disjunctions.

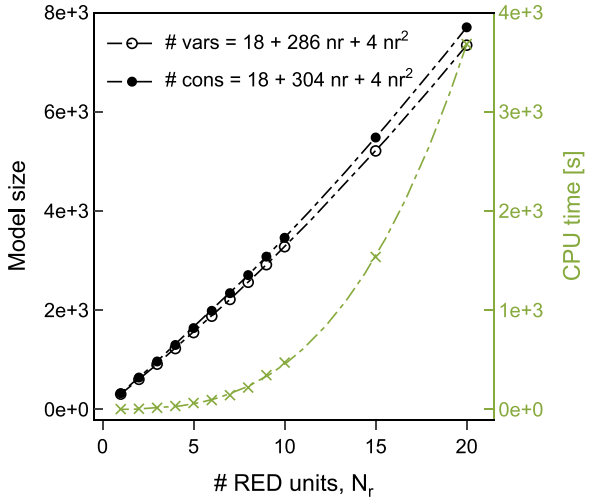

Fig. 13. Model size and solution time as a function of candidate RED units in the superstructure for the feed conditions of the illustrative example (see Table 5).

IPOPTH as local NLP solver. We access the solvers from GAMS 34.1.0 via the Pyomo-GAMS interface.

Given the complexity of the NLP subproblems, the stopping criteria depend on the maximum number of iterations of the MSNLP solver. We set 500 gradient-based NLP solver calls from multiple starting points as it suffices to guarantee a near-optimal solution. The time limit for each run is set at 1 h (3600 CPU seconds).

As expected, each RED unit added to the superstructure increases the size of the model and, as such, the time in solving the GDP problem (see Fig. 13). The most time-demanding steps are (set-covering) initial linearization of the GDP problem and solving the reduced NLP subproblems—together require almost 45% of the total solution time with four candidate RED units which scales up to ~80% with 20 RED units.

7. Conclusions

In this work, we propose a non-convex GDP model to systematically synthesize and optimize the RED process for salinity-gradient-based electricity production. We apply the GLOA algorithm to solve the GDP problem. The solution to the GDP problem provides the hydraulic topology, i.e., number of active RED units and their hydraulic arrangement, and operating conditions of each RED stack that maximize the NPV of the RED system. To illustrate the functionality of the GDP model, we defined an example with four conditional RED units. Then, we assessed two feedstreams' scenarios in an up-scaled system with ten candidate RED units. We compared the cost-optimal design in the two feed scenarios with a net-power optimal series arrangement. Even though the limited number of RED units and feed conditions render the RED process uneconomic, the optimal solution to the GDP problem in both scenarios yields more profitable designs than the conventional series staging of the RED units where the net power output is maximized. Longer lifespan of membranes and up-scaling of the RED process nameplate capacity would make the RED process profitable. Besides, the objective function can be extended, or the optimization problem reformulated into multi-objective optimization to value additional environmental and societal true benefits of RED technology towards sustainability. Our results have shown that mathematical programming techniques based on GDP are an efficient and systematic decision-making approach over simulation alone to advance full-scale RED

progress. The GDP model could be a valuable tool to assist RED field demonstration and deployment stages in real environments.

The present work laid the groundwork for subsequent modeling improvements; given the complexity and non-convex nature of the RED stack model, we will explore the development of a surrogate model to improve the computational effort and robustness of the GDP model while preserving the accuracy of our rigorous RED stack model. We will also extend the superstructure of alternatives and decision space with more discrete and continuous decision variables concerning the RED stack design (e.g., the number of cell pairs, properties of spacers and membranes) and the RED system (e.g., adding auxiliary equipment as DC-AC inverters, pre-treatment of feed solutions). We will also consider environmental and social concerns by combining multi-objective optimization and life cycle assessment methodological framework. Alternatively, monetization of the LCA results allows the integration of economic, environmental, and social criteria in the optimization process.

CRediT authorship contribution statement

C. Tristán: Conceptualization, Methodology, Software, Validation, Formal analysis, Investigation, Data curation, Writing – original draft, Visualization. **M. Fallanza:** Conceptualization, Writing – review & editing, Supervision. **R. Ibáñez:** Conceptualization, Resources, Writing – review & editing, Supervision, Project administration, Funding acquisition. **I. Ortiz:** Resources, Funding acquisition. **I.E. Grossmann:** Conceptualization, Methodology, Resources, Writing – review & editing, Supervision.

Declaration of Competing Interest

The authors declare that they have no known competing financial interests or personal relationships that could have appeared to influence the work reported in this paper.

Data availability

Data will be made available on request.

Acknowledgments

This work was supported by the LIFE Programme of the European Union (LIFE19 ENV/ES/000143); the MCIN/AEI/10.13039/501100011033 and "European Union NextGenerationEU/PRTR" (PDC2021–120786-I00); and by the MCIN/AEI/10.13039/501100011033 and "ESF Investing in your future" (PRE2018–086454).

Supplementary materials

Supplementary material associated with this article can be found, in the online version, at doi:10.1016/j.compchemeng.2023.108196.

References

Ahmetović, E., Grossmann, I.E., 2011. Global superstructure optimization for the design of integrated process water networks. AIChE J. 57, 434–457. https://doi.org/10.1002/aic.12276.

Altıok, E., Kaya, T.Z., Othman, N.H., Kınalı, O., Kitada, S., Güler, E., Kabay, N., 2022. Investigations on the effects of operational parameters in reverse electrodialysis system for salinity gradient power generation using central composite design (CCD). Desalination 525, 115508. https://doi.org/10.1016/J.DESAL.2021.115508.

Alvarez-Silva, O.A., Osorio, A.F., Winter, C., 2016. Practical global salinity gradient energy potential. Renew. Sustain. Energy Rev. 60, 1387–1395. https://doi.org/10.1016/j.rser.2016.03.021.

Butcher, J.C., 2016. Numerical Differential Equation Methods. Numerical Methods for Ordinary Differential Equations. John Wiley & Sons, Ltd, pp. 55–142. https://doi.org/10.1002/9781119121534.CH2.

Cafaro, D.C., Grossmann, I.E., 2014. Alternate approximation of concave cost functions for process design and supply chain optimization problems. Comput. Chem. Eng. 60, 376–380. https://doi.org/10.1016/J.COMPCHEMENG.2013.10.001.

Chen, Q., Johnson, E.S., Bernal, D.E., Valentin, R., Kale, S., Bates, J., Siirola, J.D., Grossmann, I.E., 2021a. Pyomo.GDP: an ecosystem for logic based modeling and optimization development. Optim. Eng. 1–36. https://doi.org/10.1007/s11081-021-09601-7.

Chen, Q., Liu, Y., Seastream, G., Siirola, J.D., Grossmann, I.E., 2021b. Pyosyn: a new framework for conceptual design modeling and optimization. Comput. Chem. Eng. 107414 https://doi.org/10.1016/J.COMPCHEMENG.2021.107414.

Ciofalo, M., La Cerva, M., Di Liberto, M., Gurreri, L., Cipollina, A., Micale, G., 2019. Optimization of net power density in reverse electrodialysis. Energy 181, 576–588. https://doi.org/10.1016/J.ENERGY.2019.05.183.

Culcasi, A., Gurreri, L., Zaffora, A., Cosenza, A., Tamburini, A., Cipollina, A., Micale, G., 2020. Ionic shortcut currents via manifolds in reverse electrodialysis stacks. Desalination 485, 114450. https://doi.org/10.1016/J.DESAL.2020.114450.

Daniilidis, A., Herber, R., Vermaas, D.A., 2014. Upscale potential and financial feasibility of a reverse electrodialysis power plant. Appl. Energy 119, 257–265. https://doi.org/10.1016/j.apenergy.2013.12.066.

Davis, S.J., Lewis, N.S., Shaner, M., Aggarwal, S., Arent, D., Azevedo, I.L., Benson, S.M., Bradley, T., Brouwer, J., Chiang, Y.M., Clack, C.T.M., Cohen, A., Doig, S., Edmonds, J., Fennell, P., Field, C.B., Hannegan, B., Hodge, B.M., Hoffert, M.I., Ingersoll, E., Jaramillo, P., Lackner, K.S., Mach, K.J., Mastrandrea, M., Ogden, J., Peterson, P.F., Sanchez, D.L., Sperling, D., Stagner, J., Trancik, J.E., Yang, C.J., Caldeira, K., 2018. Net-zero emissions energy systems. Science 360, eaas9793. https://doi.org/10.1126/SCIENCE.AAS9793, 80.

Dong, F., Jin, D., Xu, S., Wu, X., Wang, P., Wu, D., Xi, R., 2022. Three-dimensional multi-physical simulation of a reverse electrodialysis stack with profiled membranes. Desalination 537, 115894. https://doi.org/10.1016/J.DESAL.2022.115894.

Faghihi, P., Jalali, A., 2022. An artificial neural network-based optimization of reverse electrodialysis power generating cells using CFD and genetic algorithm. Int. J. Energy Res. 1–17. https://doi.org/10.1002/ER.8379.

Fraser, N.M., Jewkes, E.M., 2012. Non-Standard Annuities and Gradients, in: Engineering Economics : Financial Decision Making for Engineers. Pearson Education Canada, Toronto, pp. 65–67.

Giacalone, F., Papapetrou, M., Kosmadakis, G., Tamburini, A., Micale, G., Cipollina, A., 2019. Application of reverse electrodialysis to site-specific types of saline solutions: a techno-economic assessment. Energy 181, 532–547. https://doi.org/10.1016/j.energy.2019.05.161.

Gómez-Coma, L., Ortiz-Martínez, V.M., Carmona, J., Palacio, L., Prádanos, P., Fallanza, M., Ortiz, A., Ibañez, R., Ortiz, I., 2019. Modeling the influence of divalent ions on membrane resistance and electric power in reverse electrodialysis. J. Memb. Sci. 592, 117385 https://doi.org/10.1016/J.MEMSCI.2019.117385.

Grossmann, I.E., 2021. Basic Theoretical Concepts in Optimization. Advanced Optimization for Process Systems Engineering. Cambridge University Press, pp. 16–31. https://doi.org/10.1017/9781108917834.004.

Guillén-Gosálbez, G., You, F., Galán-Martín, Á., Pozo, C., Grossmann, I.E., 2019. Process systems engineering thinking and tools applied to sustainability problems: current landscape and future opportunities. Curr. Opin. Chem. Eng. 26, 170–179. https://doi.org/10.1016/j.coche.2019.11.002.

Gurreri, L., Tamburini, A., Cipollina, A., Micale, G., Ciofalo, M., 2017. Pressure drop at low Reynolds numbers in woven-spacer-filled channels for membrane processes: CFD prediction and experimental validation. Desalin. Water Treat. 61, 170–182. https://doi.org/10.5004/dwt.2016.11279.

Gurreri, L., Tamburini, A., Cipollina, A., Micale, G., Ciofalo, M., 2014. CFD prediction of concentration polarization phenomena in spacer-filled channels for reverse electrodialysis. J. Memb. Sci. 468, 133–148. https://doi.org/10.1016/j.memsci.2014.05.058.

Hart, W.E., Laird, C.D., Watson, J.P., Woodruff, D.L., Hackebeil, G.A., Nicholson, B.L., Siirola, J.D., 2017. Pyomo — Optimization Modeling in Python, Second Edi. ed, Springer Optimization and Its Applications. Springer International Publishing, Cham. https://doi.org/10.1007/978-3-319-58821-6.

Hu, J., Xu, S., Wu, X., Wang, S., Zhang, X., Yang, S., Xi, R., Wu, D., Xu, L., 2020. Experimental investigation on the performance of series control multi-stage reverse electrodialysis. Energy Convers. Manag. 204, 112284 https://doi.org/10.1016/J.ENCONMAN.2019.112284.

Hu, J., Xu, S., Wu, X., Wu, D., Jin, D., Wang, P., Leng, Q., 2019. Multi-stage reverse electrodialysis: strategies to harvest salinity gradient energy. Energy Convers. Manag. 183, 803–815. https://doi.org/10.1016/J.ENCONMAN.2018.11.032.

IEA, 2016. Water-Energy Nexus. IEA, Paris. reports/water-energy-nexus.

IRENA, 2020. Innovation outlook: Ocean energy Technologies. International Renewable Energy Agency, Abu Dhabi.

IRENA, 2022. Renewable power generation costs in 2021. International Renewable Energy Agency, Abu Dhabi.

Jang, J., Kang, Y., Han, J.H., Jang, K., Kim, C.M., Kim, I.S., 2020. Developments and future prospects of reverse electrodialysis for salinity gradient power generation: influence of ion exchange membranes and electrodes. Desalination 491, 114540. https://doi.org/10.1016/j.desal.2020.114540.

Karuppiah, R., Grossmann, I.E., 2006. Global optimization for the synthesis of integrated water systems in chemical processes. Comput. Chem. Eng. 30, 650–673. https://doi.org/10.1016/j.compchemeng.2005.11.005.

Kempener, R., Neumann, F., 2014. Salinity Gradient Energy Technology Brief. IRENA Ocean Energy Technol.

Kim, M., Kim, S., Choi, J., Kim, H., Jeong, N., Kwak, R., 2022. Numerical analysis of real-scale reverse electrodialysis with microscale structures and electrode segmentation. Chem. Eng. J. 446, 137357 https://doi.org/10.1016/J.CEJ.2022.137357.

Kravanja, Z., Čuček, L., 2013. Multi-objective optimisation for generating sustainable solutions considering total effects on the environment. Appl. Energy 101, 67–80. https://doi.org/10.1016/J.APENERGY.2012.04.025.

Krey, V., Masera, O., Blanforde, G., Bruckner, T., Cooke, R., Fish-Vanden, K., Haberl, H., Hertwich, E., Kriegler, E., Müller, D., Paltsev, S., Price, L., Schlömer, S., Uerge-Vorsatz, D., Van Vuuren, D., Zwickel, T., Edenhofer, O., Pichs-Madruga, R., Sokona, Y., Farahani, E., Kadner, S., Seyboth, K., Adler, A., Baum, I., Brunner, S., Eickemeier, P., Kriemann, B., Savolainen, J., Schömer, S., Von Stechow, C., Zwickel, T., Minx, J.C., 2014. Annex II: metrics & methodology. Eds Climate Change 2014: Mitigation of Climate Change. Contribution of Working Group III to the Fifth Assessment Report of the Intergovernmental Panel On Climate Change. Cambridge University Press, Cambridge, United Kingdom, pp. 1281–1328.

Kuleszo, J., Kroeze, C., Post, J., Fekete, B.M., 2010. The potential of blue energy for reducing emissions of CO_2 and non-CO_2 greenhouse gases. J. Integr. Environ. Sci. 7, 89–96. https://doi.org/10.1080/19438151003680850.

La-Cerva, M.L., Liberto, M.Di, Gurreri, L., Tamburini, A., Cipollina, A., Micale, G., Ciofalo, M., 2017. Coupling CFD with a one-dimensional model to predict the performance of reverse electrodialysis stacks. J. Memb. Sci. 541, 595–610. https://doi.org/10.1016/j.memsci.2017.07.030.

Lacey, R.E., 1980. Energy by reverse electrodialysis. Ocean Eng 7, 1–47. https://doi.org/10.1016/0029-8018(80)90030-X.

Lee, S., Grossmann, I.E., 2001. A global optimization algorithm for nonconvex generalized disjunctive programming and applications to process systems. Comput. Chem. Eng. 25, 1675–1697. https://doi.org/10.1016/S0098-1354(01)00732-3.

Logan, B.E., Elimelech, M., 2012. Membrane-based processes for sustainable power generation using water. Nature 488, 313–319. https://doi.org/10.1038/nature11477.

Long, R., Li, B., Liu, Z., Liu, W., 2018a. Reverse electrodialysis: modelling and performance analysis based on multi-objective optimization. Energy 151, 1–10. https://doi.org/10.1016/j.energy.2018.03.003.

Long, R., Li, B., Liu, Z., Liu, W., 2018b. Performance analysis of reverse electrodialysis stacks: channel geometry and flow rate optimization. Energy 158, 427–436. https://doi.org/10.1016/J.ENERGY.2018.06.067.

Makabe, R., Ueyama, T., Sakai, H., Tanioka, A., 2021. Commercial pressure retarded osmosis systems for seawater desalination plants. Member 11, 69. https://doi.org/10.3390/MEMBRANES11010069, 2021Page11, 69.

Mehdizadeh, S., Kakihana, Y., Abo, T., Yuan, Q., Higa, M., 2021. Power generation performance of a pilot-scale reverse electrodialysis using monovalent selective ion-exchange membranes. Membranes 11, 27. https://doi.org/10.3390/MEMBRANES11010027. Basel.

Nam, J.Y., Hwang, K.S., Kim, H.C., Jeong, H., Kim, H., Jwa, E., Yang, S., Choi, J., Kim, C. S., Han, J.H., Jeong, N., 2019. Assessing the behavior of the feed-water constituents of a pilot-scale 1000-cell-pair reverse electrodialysis with seawater and municipal wastewater effluent. Water Res. 148, 261–271. https://doi.org/10.1016/J.WATRES.2018.10.054.

Nicholson, B., Siirola, J.D., Watson, J.P., Zavala, V.M., Biegler, L.T., 2017. pyomo.dae : a modeling and automatic discretization framework for optimization with differential and algebraic equations. Math. Program. Comput. 102 (10), 187–223. https://doi.org/10.1007/S12532-017-0127-0, 2017.

Ortiz-Imedio, R., Gomez-Coma, L., Fallanza, M., Ortiz, A., Ibañez, R., Ortiz, I., 2019. Comparative performance of Salinity Gradient Power-Reverse Electrodialysis under different operating conditions. Desalination 457, 8–21. https://doi.org/10.1016/J.DESAL.2019.01.005.

Ortiz-Martínez, V.M., Gómez-Coma, L., Tristán, C., Pérez, G., Fallanza, M., Ortiz, A., Ibañez, R., Ortiz, I., 2020. A comprehensive study on the effects of operation variables on reverse electrodialysis performance. Desalination 482, 114389. https://doi.org/10.1016/J.DESAL.2020.114389.

Papalambros, P.Y., Wilde, D.J., 2018. Model Boundedness, in: Principles of Optimal Design. Cambridge University Press, pp. 91–161. https://doi.org/10.1017/9781316451038.004.

Papapetrou, M., Kosmadakis, G., Giacalone, F., Ortega-Delgado, B., Cipollina, A., Tamburini, A., Micale, G., 2019. Evaluation of the economic and environmental performance of low-temperature heat to power conversion using a reverse electrodialysis – multi-effect distillation system. Energies 12, 3206. https://doi.org/10.3390/en12173206.

Pärnamäe, R., Gurreri, L., Post, J., Van Egmond, W.J., Culcasi, A., Saakes, M., Cen, J., Goosen, E., Tamburini, A., Vermaas, D.A., Tedesco, M., 2020. The acid–base flow battery: sustainable energy storage via reversible water dissociation with bipolar membranes. Membranes 10, 409. https://doi.org/10.3390/MEMBRANES10120409. Basel.

Pattle, R.E., 1954. Production of Electric Power by mixing Fresh and Salt Water in the Hydroelectric Pile. Nature 174, 660. https://doi.org/10.1038/174660a0. –660.

Pawlowski, S., Geraldes, V., Crespo, J.G., Velizarov, S., 2016. Computational fluid dynamics (CFD) assisted analysis of profiled membranes performance in reverse electrodialysis. J. Memb. Sci. 502, 179–190. https://doi.org/10.1016/j.memsci.2015.11.031.

Pieragostini, C., Mussati, M.C., Aguirre, P., 2012. On process optimization considering LCA methodology. J. Environ. Manage. 96, 43–54. https://doi.org/10.1016/J.JENVMAN.2011.10.014.

Pintossi, D., Simões, C., Saakes, M., Borneman, Z., Nijmeijer, K., 2021. Predicting reverse electrodialysis performance in the presence of divalent ions for renewable energy generation. Energy Convers. Manag. 243, 114369 https://doi.org/10.1016/J.ENCONMAN.2021.114369.

Pistikopoulos, E.N., Barbosa-Povoa, A., Lee, J.H., Misener, R., Mitsos, A., Reklaitis, G.V., Venkatasubramanian, V., You, F., Gani, R., 2021. Process systems engineering – The generation next? Comput. Chem. Eng. 147, 107252 https://doi.org/10.1016/j.compchemeng.2021.107252.

Pizzol, M., Weidema, B., Brandão, M., Osset, P., 2015. Monetary valuation in life cycle assessment: a review. J. Clean. Prod. 86, 170–179. https://doi.org/10.1016/j.jclepro.2014.08.007.

Post, J.W., Goeting, C.H., Valk, J., Goinga, S., Veerman, J., Hamelers, H.V.M., Hack, P.J. F.M., 2010. Towards implementation of reverse electrodialysis for power generation from salinity gradients. Desalin. Water Treat. 16, 182–193. https://doi.org/10.5004/dwt.2010.1093.

Post, J.W., Hamelers, H.V.M., Buisman, C.J.N., 2008. Energy recovery from controlled mixing salt and fresh water with a reverse electrodialysis system. Environ. Sci. Technol. 42, 5785–5790. https://doi.org/10.1021/es8004317.

Quesada, I., Grossmann, I.E., 1995. Global optimization of bilinear process networks with multicomponent flows. Comput. Chem. Eng. 19, 1219–1242. https://doi.org/10.1016/0098-1354(94)00123-5.

Ramon, G.Z., Feinberg, B.J., Yu, Z.L.T., Hoek, E.M.V., 2011. Membrane-based production of salinity-gradient power. Energy Environ. Sci. 4, 4423–4434. https://doi.org/10.1039/c1ee01913a.

Rani, A., Snyder, S.W., Kim, H., Lei, Z., Pan, S.Y., 2022. Pathways to a net-zero-carbon water sector through energy-extracting wastewater technologies. Npj Clean Water 51 (5), 1–17. https://doi.org/10.1038/s41545-022-00197-8, 2022.

Simões, C., Pintossi, D., Saakes, M., Borneman, Z., Brilman, W., Nijmeijer, K., 2020. Electrode segmentation in reverse electrodialysis: improved power and energy efficiency. Desalination 492, 114604. https://doi.org/10.1016/j.desal.2020.114604.

Simões, C., Pintossi, D., Saakes, M., Brilman, W., 2021. Optimizing multistage reverse electrodialysis for enhanced energy recovery from river water and seawater: experimental and modeling investigation. Adv. Appl. Energy 2, 100023. https://doi.org/10.1016/J.ADAPEN.2021.100023.

Simões, C., Vital, B., Sleutels, T., Saakes, M., Brilman, W., 2022. Scaled-up multistage reverse electrodialysis pilot study with natural waters. Chem. Eng. J. 450, 138412 https://doi.org/10.1016/J.CEJ.2022.138412.

Sinnott, R., Towler, G., Sinnott, R., Towler, G., 2020. Costing and project evaluation. Eds Chemical Engineering Design, Chemical Engineering. Elsevier, pp. 275–369. https://doi.org/10.1016/b978-0-08-102599-4.00006-0.

Tedesco, M., Cipollina, A., Tamburini, A., Bogle, I.D.L., Micale, G., 2015a. A simulation tool for analysis and design of reverse electrodialysis using concentrated brines. Chem. Eng. Res. Des. 93, 441–456. https://doi.org/10.1016/j.cherd.2014.05.009.

Tedesco, M., Cipollina, A., Tamburini, A., Micale, G., 2017. Towards 1kW power production in a reverse electrodialysis pilot plant with saline waters and concentrated brines. J. Memb. Sci. 522, 226–236. https://doi.org/10.1016/j.memsci.2016.09.015.

Tedesco, M., Mazzola, P., Tamburini, A., Micale, G., Bogle, I.D.L., Papapetrou, M., Cipollina, A., 2015b. Analysis and simulation of scale-up potentials in reverse electrodialysis. Desalin. Water Treat. 55, 3391–3403. https://doi.org/10.1080/19443994.2014.947781.

Tian, H., Wang, Y., Pei, Y., Crittenden, J.C., 2020. Unique applications and improvements of reverse electrodialysis: a review and outlook. Appl. Energy 262, 114482. https://doi.org/10.1016/J.APENERGY.2019.114482.

Tristán, C., Fallanza, M., Ibáñez, R., Ortiz, I., 2020a. Recovery of salinity gradient energy in desalination plants by reverse electrodialysis. Desalination 496, 114699. https://doi.org/10.1016/j.desal.2020.114699.

Tristán, C., Fallanza, M., Ibáñez, R., Ortiz, I., 2020b. Reverse electrodialysis: potential reduction in energy and emissions of desalination. Appl. Sci. 10, 1–21. https://doi.org/10.3390/app10207317.

Tufa, R.A., Pawlowski, S., Veerman, J., Bouzek, K., Fontananova, E., di Profio, G., Velizarov, S., Goulão Crespo, J., Nijmeijer, K., Curcio, E., 2018. Progress and prospects in reverse electrodialysis for salinity gradient energy conversion and storage. Appl. Energy 225, 290–331. https://doi.org/10.1016/J.APENERGY.2018.04.111.

UNESCO, 2020. UN-Water, 2020: United Nations World Water Development Report 2020: Water and Climate Change. UNESCO, Paris.

Van Vliet, M.T.H., Jones, E.R., Flörke, M., Franssen, W.H.P., Hanasaki, N., Wada, Y., Yearsley, J.R., 2021. Global water scarcity including surface water quality and expansions of clean water technologies. Environ. Res. Lett. 16, 024020 https://doi.org/10.1088/1748-9326/ABBFC3.

Veerman, J., 2020. Reverse electrodialysis: co-and counterflow optimization of multistage configurations for maximum energy efficiency. Membranes 10, 1–13. https://doi.org/10.3390/membranes10090206. Basel.

Veerman, J., Post, J.W., Saakes, M., Metz, S.J., Harmsen, G.J., 2008. Reducing power losses caused by ionic shortcut currents in reverse electrodialysis stacks by a validated model. J. Memb. Sci. 310, 418–430. https://doi.org/10.1016/j.memsci.2007.11.032.

Veerman, J., Saakes, M., Metz, S.J., Harmsen, G.J., 2011. Reverse electrodialysis: a validated process model for design and optimization. Chem. Eng. J. 166, 256–268. https://doi.org/10.1016/j.cej.2010.10.071.

Veerman, J., Saakes, M., Metz, S.J., Harmsen, G.J., 2009. Reverse electrodialysis: performance of a stack with 50 cells on the mixing of sea and river water. J. Memb. Sci. 327, 136–144. https://doi.org/10.1016/j.memsci.2008.11.015.

Vermaas, D.A., Veerman, J., Yip, N.Y., Elimelech, M., Saakes, M., Nijmeijer, K., 2013. High efficiency in energy generation from salinity gradients with reverse electrodialysis. ACS Sustain. Chem. Eng. 1, 1295–1302. https://doi.org/10.1021/sc400150w.

Weiner, A.M., McGovern, R.K., Lienhard V, J.H., 2015. Increasing the power density and reducing the levelized cost of electricity of a reverse electrodialysis stack through blending. Desalination 369, 140–148. https://doi.org/10.1016/j.desal.2015.04.031.

Weinstein, J.N., Leitz, F.B., 1976. Electric power from differences in salinity: the dialytic battery. Science 191, 557–559. https://doi.org/10.1126/science.191.4227.557, 80.

Yip, N.Y., Brogioli, D., Hamelers, H.V.M., Nijmeijer, K., 2016. Salinity gradients for sustainable energy: primer, progress, and prospects. Environ. Sci. Technol. 50, 12072–12094. https://doi.org/10.1021/acs.est.6b03448.